Dynamic Construction of a Durable Epitaxial Catalytic Layer for Industrial Alkaline Water Splitting

Bin Chang,[1,2,3,#] Xiaoyan Liu,[1,#] Shouwei Zuo,[2,4,#] Yuanfu Ren,[2,3] Jietong He,[1] Daqing Wang,[5] Yongjiu Lei,[2] Miao Hu,[2,3] Wan-Lu Li,[6] Mohd Adnan Khan,[7] Rashed Aleisa,[7] Riming Hu,[8] Yang Hou,[9] Hong Liu,[1,10] Weijia Zhou,[1,*] Zhiping Lai,[2] Husam N. Alshareef,[2] Huabin Zhang[2,3*]

[1]*Institute for Advanced Interdisciplinary Research (IAIR), School of Chemistry and Chemical Engineering, University of Jinan, Jinan, 250022, P. R. China.*

[2] *Center for Renewable Energy and Storage Technologies (CREST), Physical Science and Engineering Division, King Abdullah University of Science and Technology (KAUST), Thuwal, 23955-6900, Kingdom of Saudi Arabia.*

[3]*KAUST Catalysis Center (KCC), Division of Physical Science and Engineering, King Abdullah University of Science and Technology (KAUST), Thuwal, 23955-6900 Kingdom of Saudi Arabia.*

[4]*State Key Laboratory of Petroleum Molecular & Process Engineering, Shanghai Key Laboratory of Green Chemistry and Chemical Processes, School of Chemistry and Molecular Engineering, East China Normal University, Shanghai 200062, P. R. China.*

[5] *Research Institute for Advanced Manufacturing, Department of Industrial and Systems Engineering, The Hong Kong Polytechnic University, Kowloon, Hong Kong, SAR, 999007, P. R. China.*

[6] *Aiiso Yufeng Li Family Department of Chemical and Nano Engineering, University of California San Diego, La Jolla, 92093, USA.*

[7] *Sustainable Fuels and Chemicals Team, Saudi Aramco Research and Development Center, Dhahran, 31311, Kingdom of Saudi Arabia.*

[8]*Institute for Smart Materials & Engineering, University of Jinan, Jinan, P. R. China.*

[9]*Key Laboratory of Biomass Chemical Engineering of Ministry of Education, College of Chemical and Biological Engineering, Zhejiang University, Hangzhou 310027, P. R. China.*

[10]*State Key Laboratory of Crystal Materials, Shandong University, Jinan, 250100, P. R. China.*

[#] These authors contributed equally to this work.

* Corresponding E-mail: ifc_zhouwj@ujn.edu.cn; huabin.zhang@kaust.edu.sa

Supplementary Figures

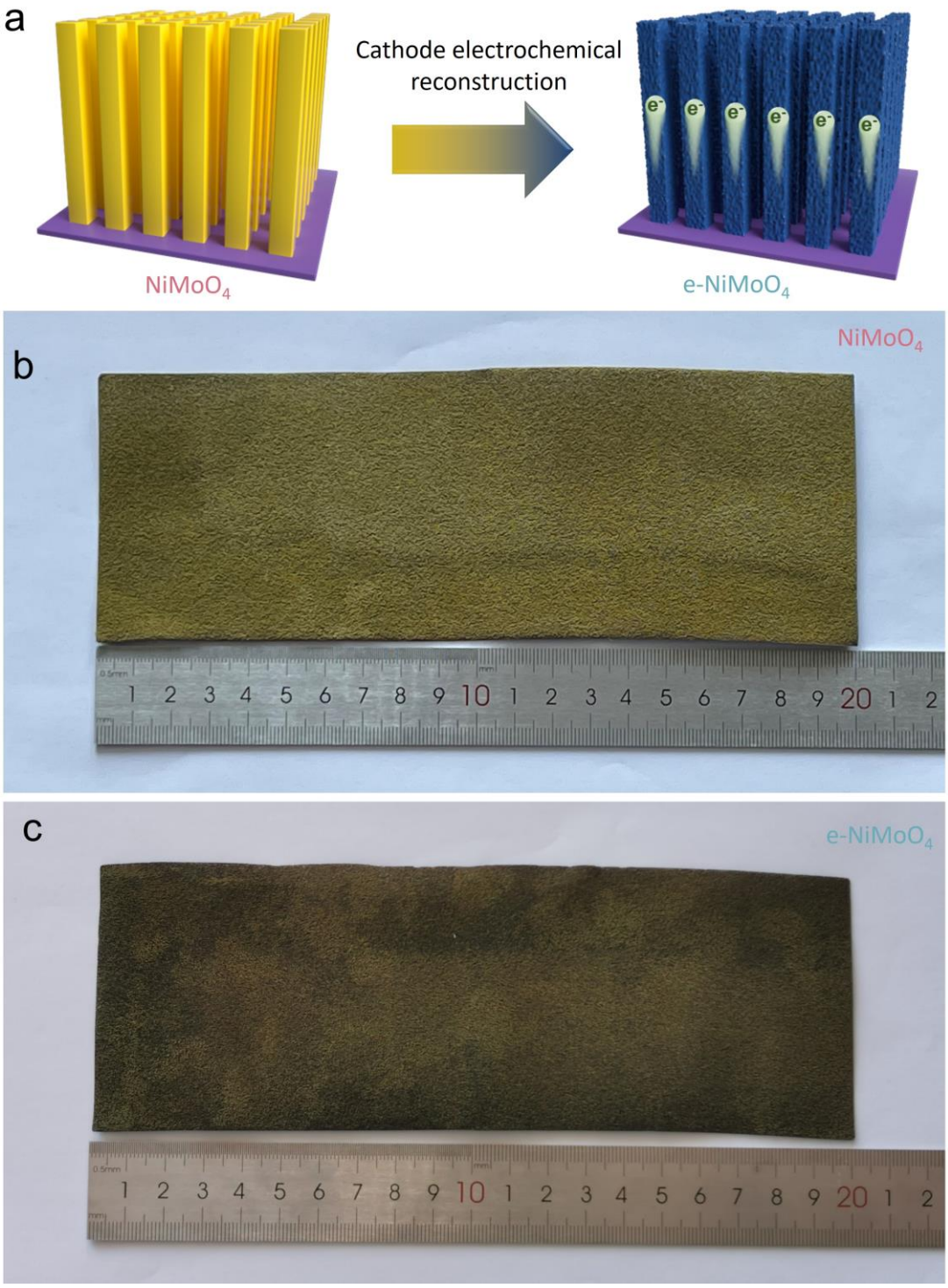

Supplementary Fig. 1 a, Scheme of e-$NiMoO_4$ synthesis. **b,** Photograph of $NiMoO_4$ electrode. **c,** Photograph of e-$NiMoO_4$ electrode.

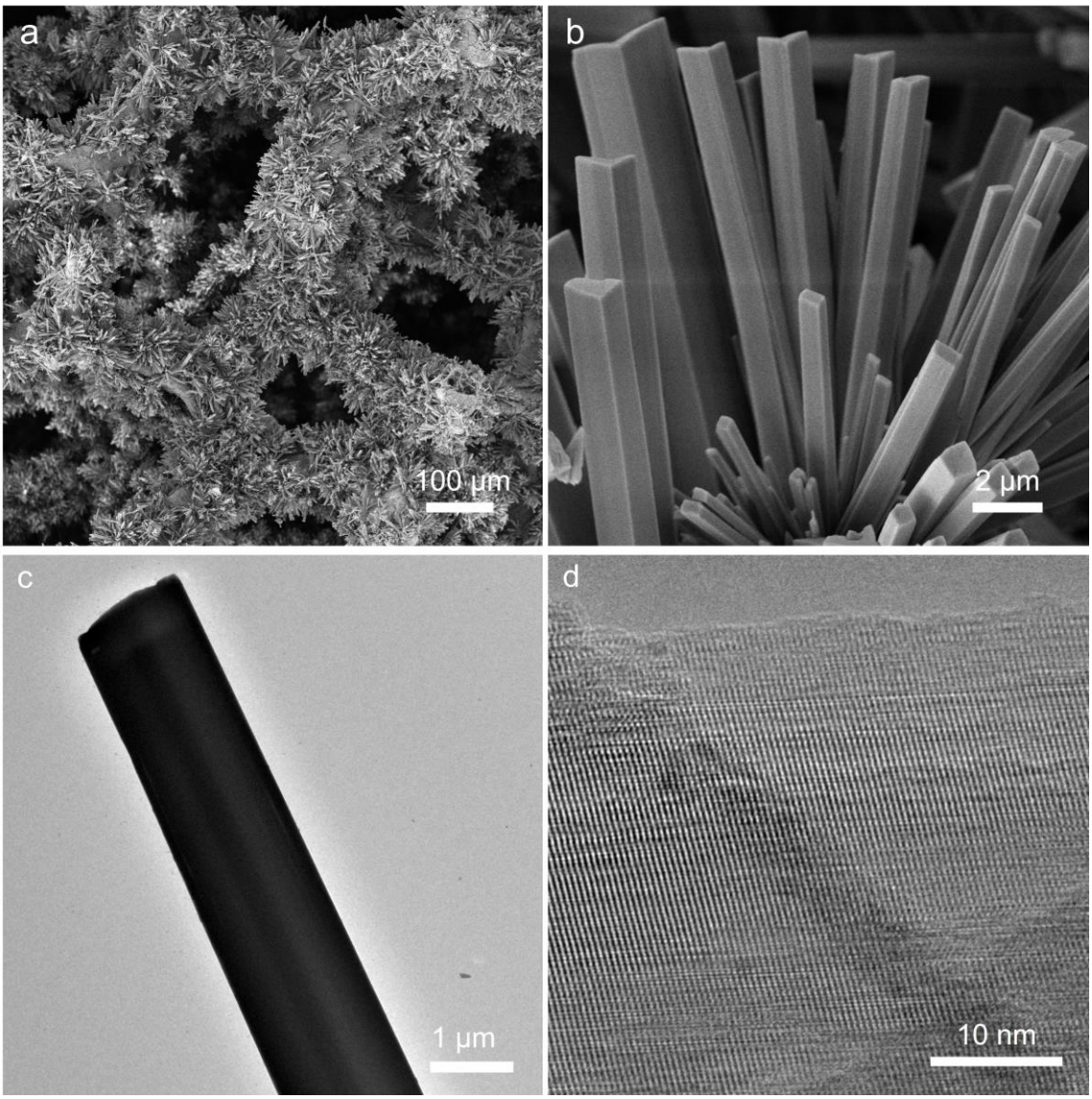

Supplementary Fig. 2 a, b, SEM image of $NiMoO_4$ at different magnification. **c,** TEM image of $NiMoO_4$. **d,** HRTEM image of $NiMoO_4$.

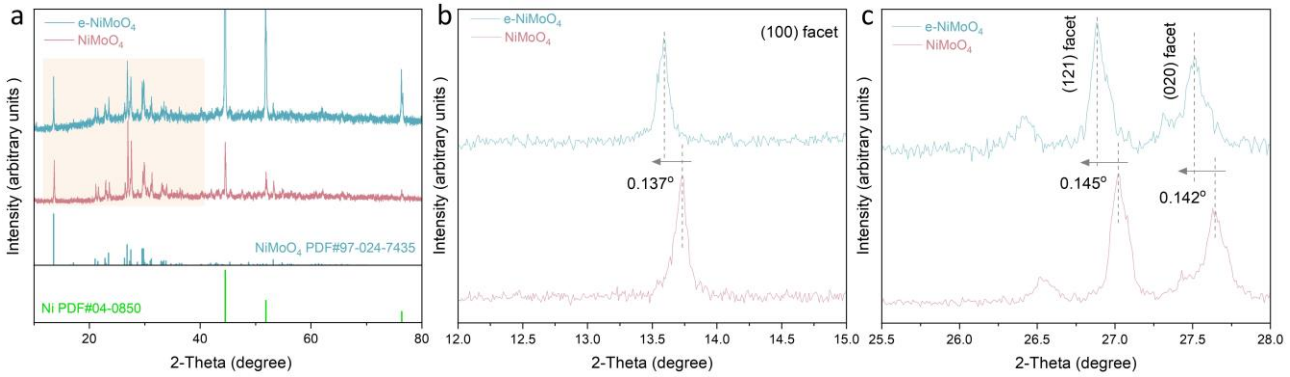

Supplementary Fig. 3 a, XRD patterns of e-$NiMoO_4$ and $NiMoO_4$. **b, c,** The corresponding enlarged area of XRD patterns.

During the epitaxial growth of the hydroxide layer on the $NiMoO_4$ surface, the newly formed interface generates stress, which propagates into the $NiMoO_4$ lattice, causing slight lattice expansion and distortion. Consequently, the formation of the surface hydroxide layer may alter the d-spacing of the original $NiMoO_4$ core structure, leading to a negative shift in the XRD peak positions[1, 2].

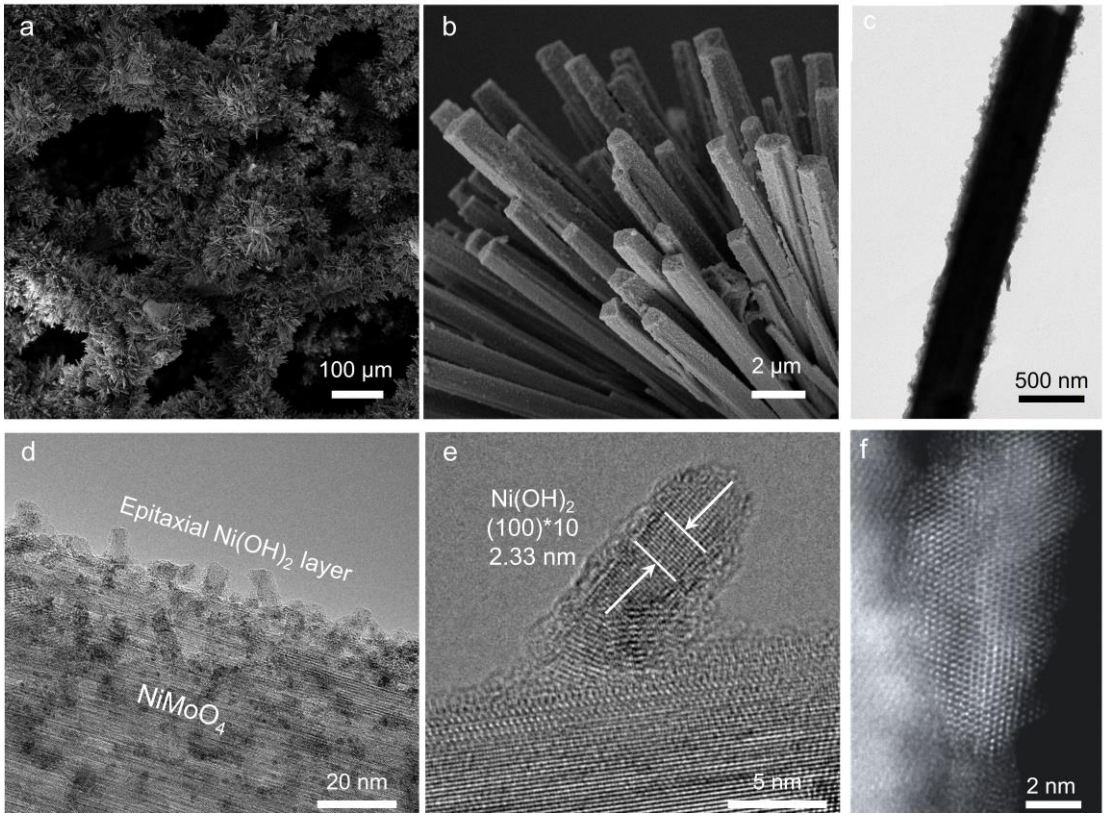

Supplementary Fig. 4 a, b, SEM image of e-$NiMoO_4$ at different magnification. **c,** TEM image of e-$NiMoO_4$. **d, e,** HRTEM image of e-$NiMoO_4$ at different magnification. **f,** High-resolution HAADF-STEM image of e-$NiMoO_4$.

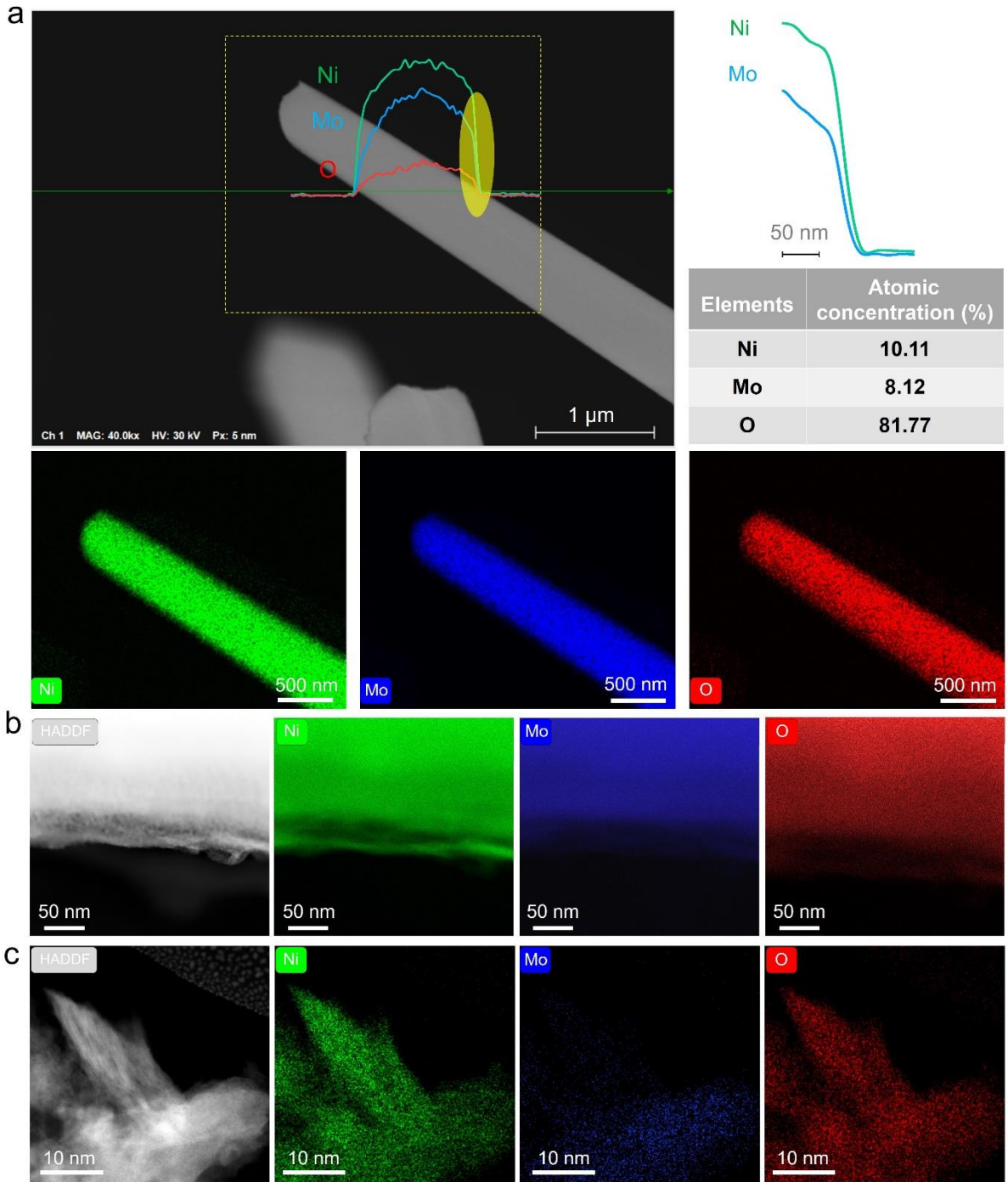

Supplementary Fig. 5 a, EDS elemental mapping with cross-sectional line scanning. **b**, HRTEM elemental mapping. **c**, HAADF- STEM elemental mapping.

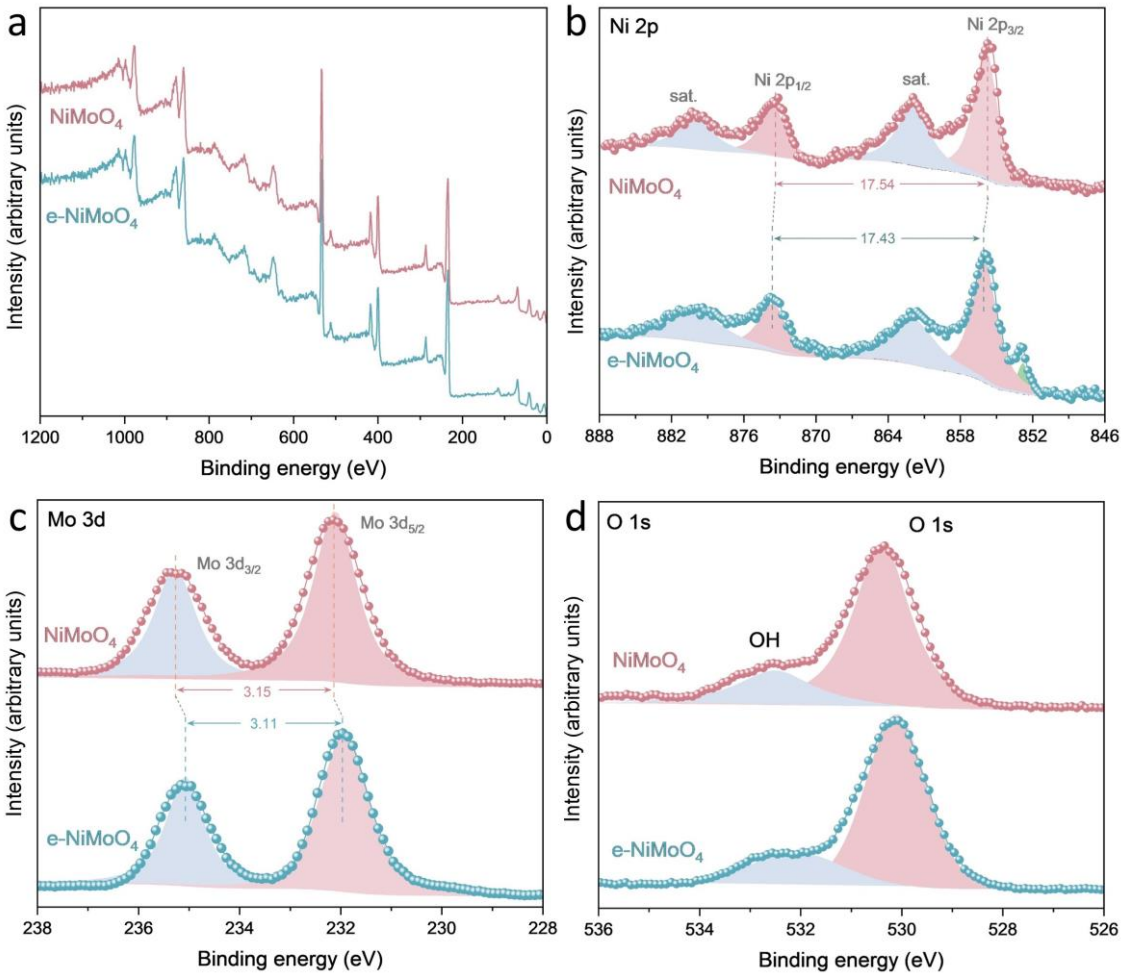

Supplementary Fig. 6 a, Survey spectra of $NiMoO_4$ and e-$NiMoO_4$, **b,** Corresponding high-resolution Ni 2p spectra. **c,** Corresponding high-resolution Mo 3d spectra. **d,** Corresponding high-resolution O 1s spectra.

After the electrochemical synthesis and the introduction of $Ni(OH)_2$, the oxidation state of Ni nearly remains unchanged, while that of Mo shifts significantly toward a lower valence state[3]. This observation aligns with the growth mechanism, which involves the balance between surface Mo leaching and the epitaxial growth of $Ni(OH)_2$. Furthermore, the interfacial coupling between $Ni(OH)_2$ and $NiMoO_4$ increases the electron density at the oxygen sites, resulting in a negative shift of the O 1s peak from 531.5 eV to 531.2 eV.

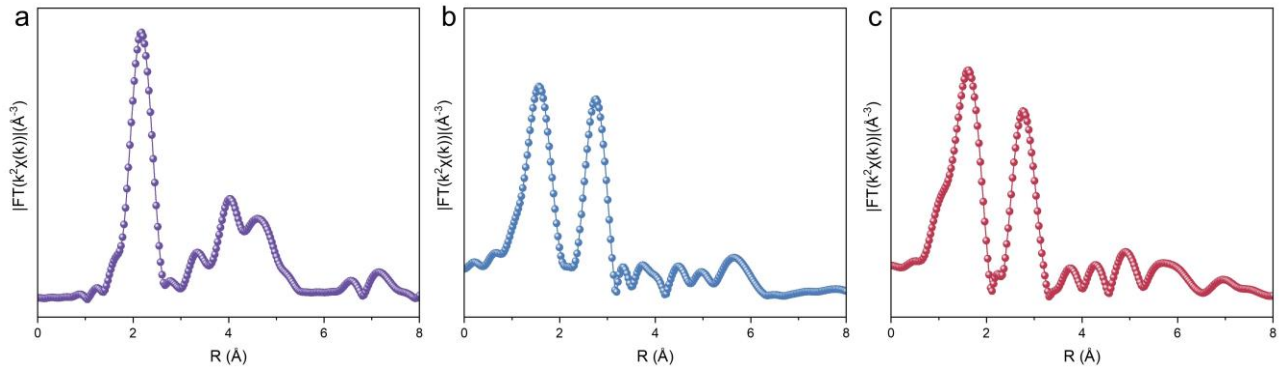

Supplementary Fig. 7 EXAFS spectra in R space for Ni K-edge of Ni foil (**a**), $Ni(OH)_2$ (**b**) and NiOOH (**c**).

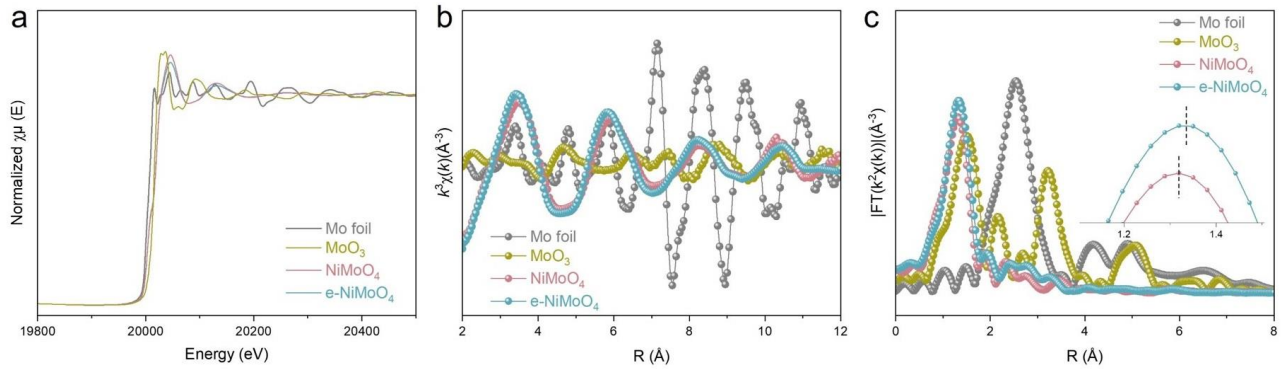

Supplementary Fig. 8 a, Mo K-edge XANES spectra of NiMoO4, e-NiMoO4, Mo foil and MoO3. **b,** The corresponding k space for Mo K-edge. **c,** The corresponding Fourier transformed magnitudes of Mo K-edge EXAFS spectra.

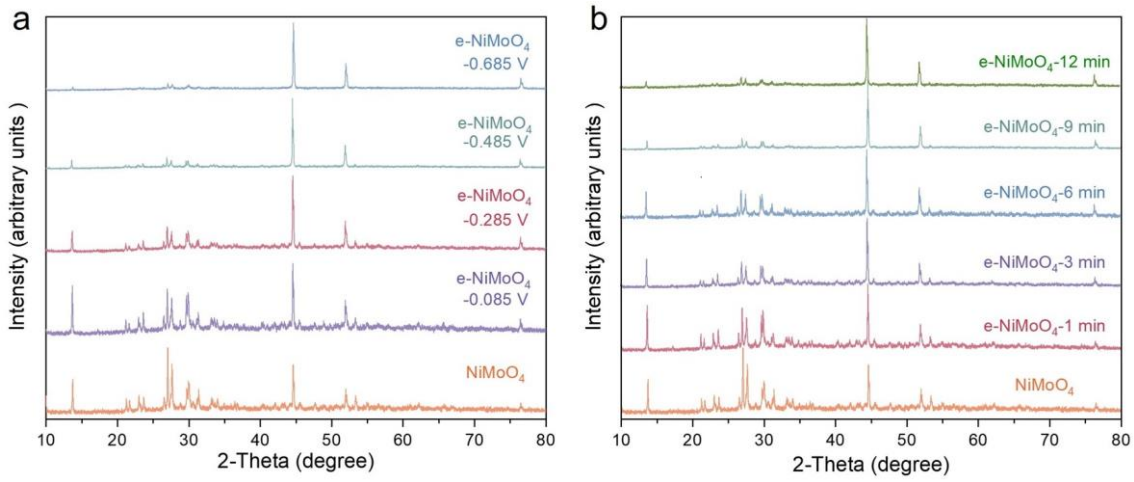

Supplementary Fig. 9 a, e-$NiMoO_4$ with different reconstruction potential. **b,** e-$NiMoO_4$ with different reconstruction time.

With higher voltages, there is a tendency for microrods to collapse. Meanwhile, prolonged synthesis times lead to increased etching depth, emphasizing the controllable epitaxial growth of nickel hydroxides layer.

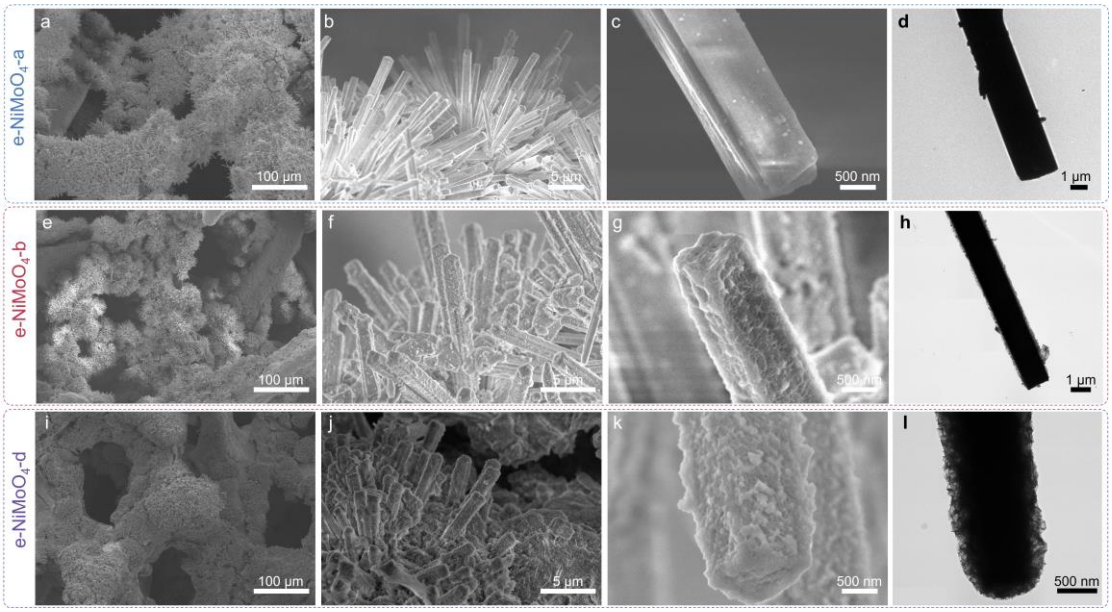

Supplementary Fig. 10 a, b, c, SEM images of e-$NiMoO_4$-a (-0.085 V) at different magnification. **d,** TEM image of e-$NiMoO_4$-a (-0.085 V). **e, f, g,** SEM images of e-$NiMoO_4$-a (-0.285 V) at different magnification. **h,** TEM image of e-$NiMoO_4$-a (-0.285 V). **i, j, k,** SEM images of e-$NiMoO_4$-a (-0.685 V) at different magnification. **l,** TEM image of e-$NiMoO_4$-a (-0.685 V).

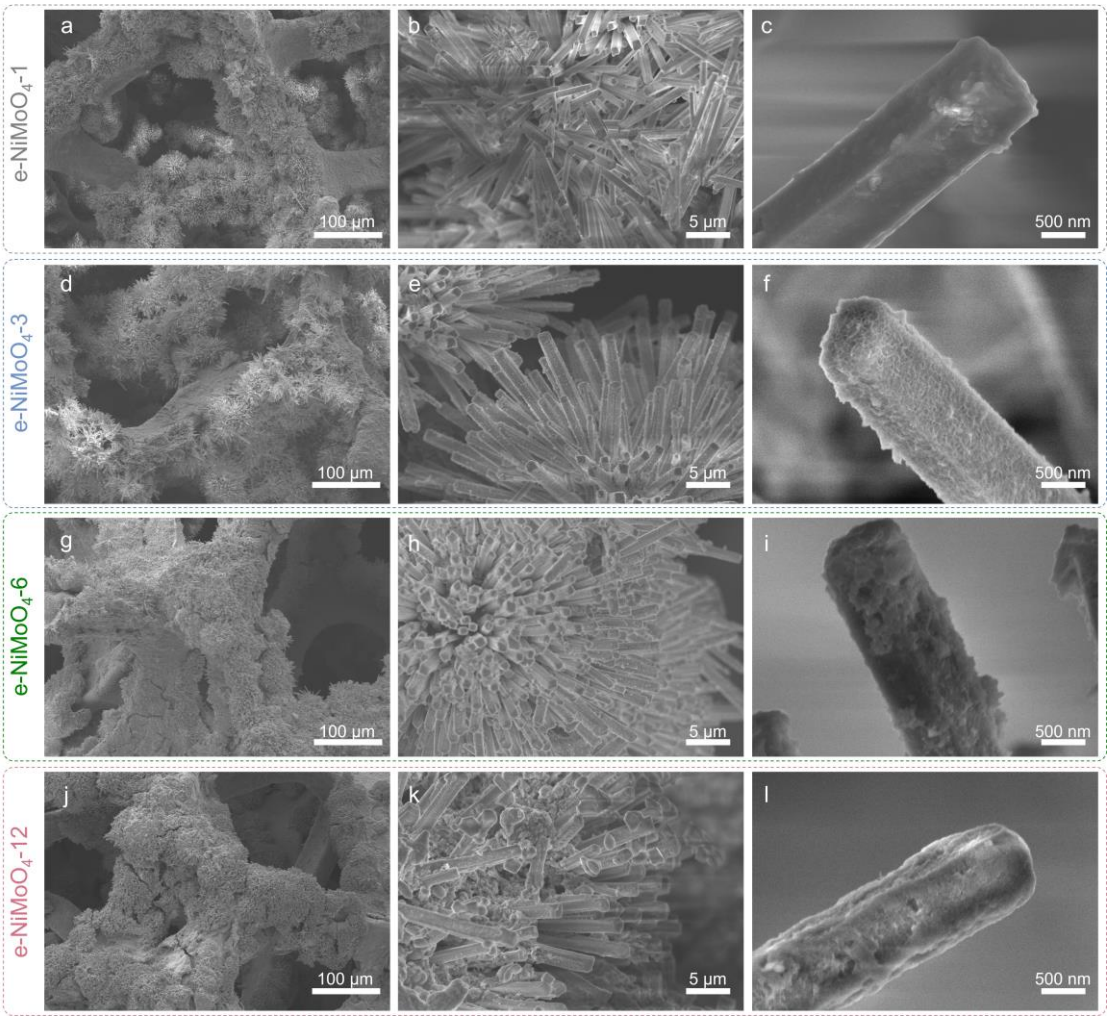

Supplementary Fig. 11 a, b, c, SEM images of e-$NiMoO_4$-1 (1min) at different magnifications. **d, e, f,** SEM images of e-$NiMoO_4$-3 (3min) at different magnification. **g, h, i,** SEM images of e-$NiMoO_4$-6 (6min) at different magnification. **j, k, l,** SEM images of e-$NiMoO_4$-1 (12min) at different magnification.

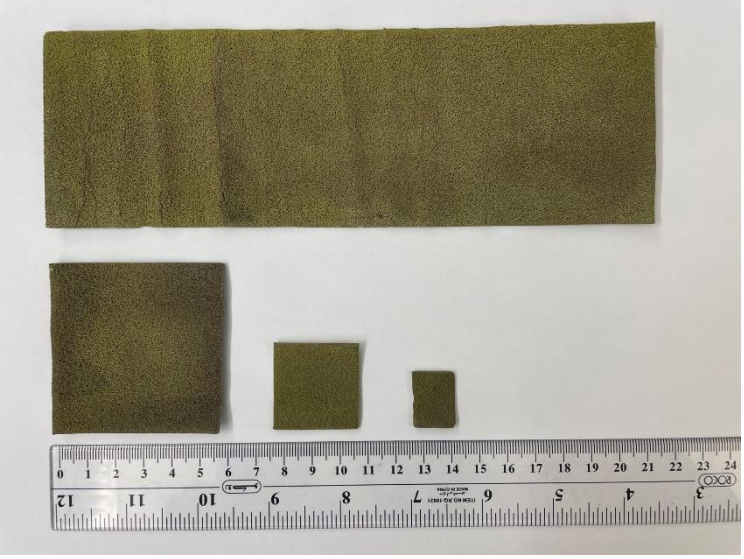

Supplementary Fig. 12 Photograph of e-$NiMoO_4$ electrode with different sizes.

The current density was precisely controlled by proportionally adjusting the total current using a DC power supply. A uniform current density of 200 mA/cm² was maintained across all electrode sizes to prevent localized overpotential effects[4]. For large-scale electrode reconstruction systems, a peristaltic pump-driven circulation system was employed to regulate dynamic electrolyte flow, mitigating mass transport limitations, minimizing concentration polarization, and maintaining temperature stability. This approach ensured uniform ion distribution and local pH stability during the reconstruction process, ultimately enabling the optimized synthesis of electrodes with various sizes.

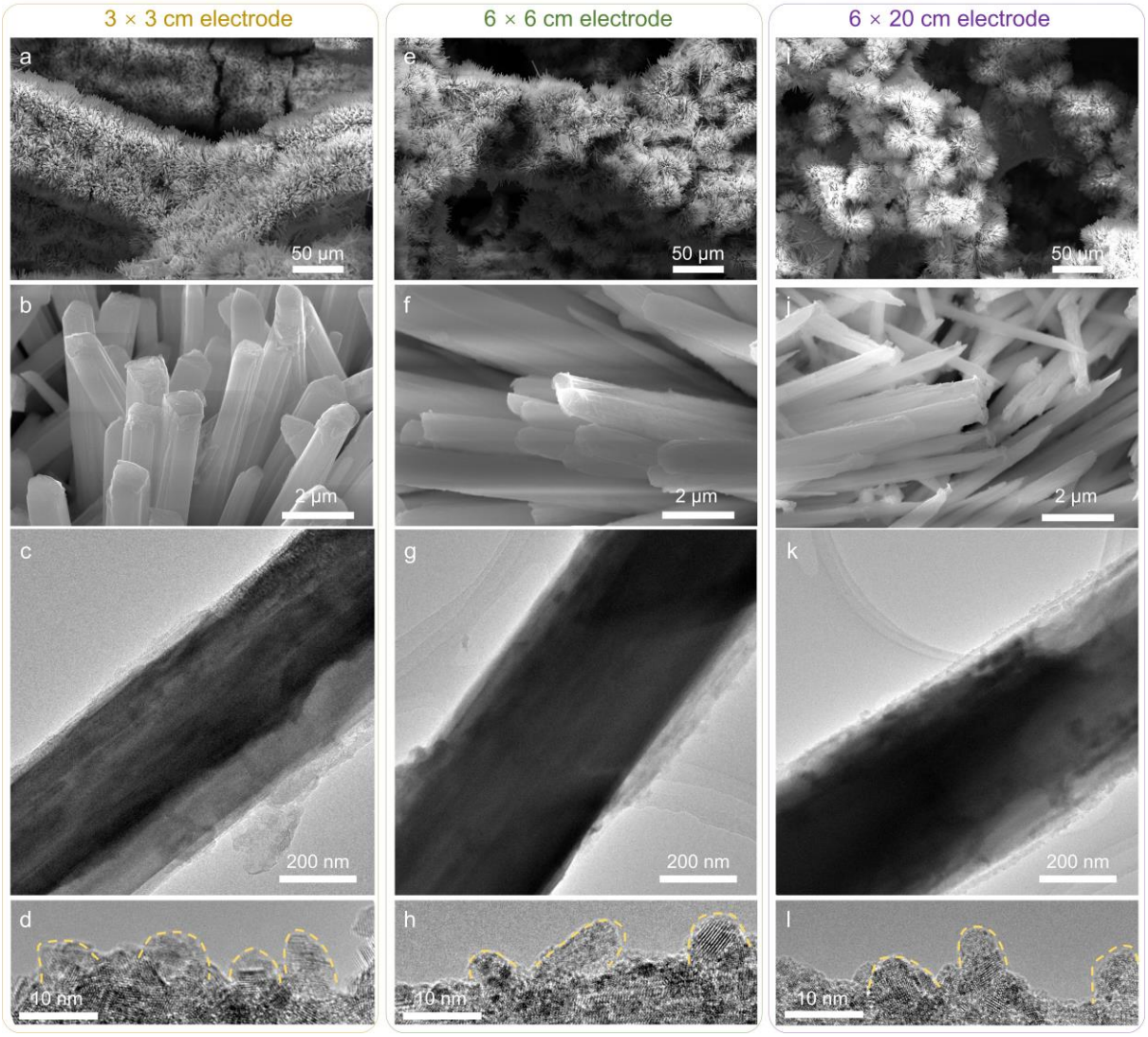

Supplementary Fig. 13 a, b, e, f, i, j SEM images of e-$NiMoO_4$ with different sizes at different magnifications. **c, d, g, h, k, l** TEM images of e-$NiMoO_4$ with different sizes at different magnifications.

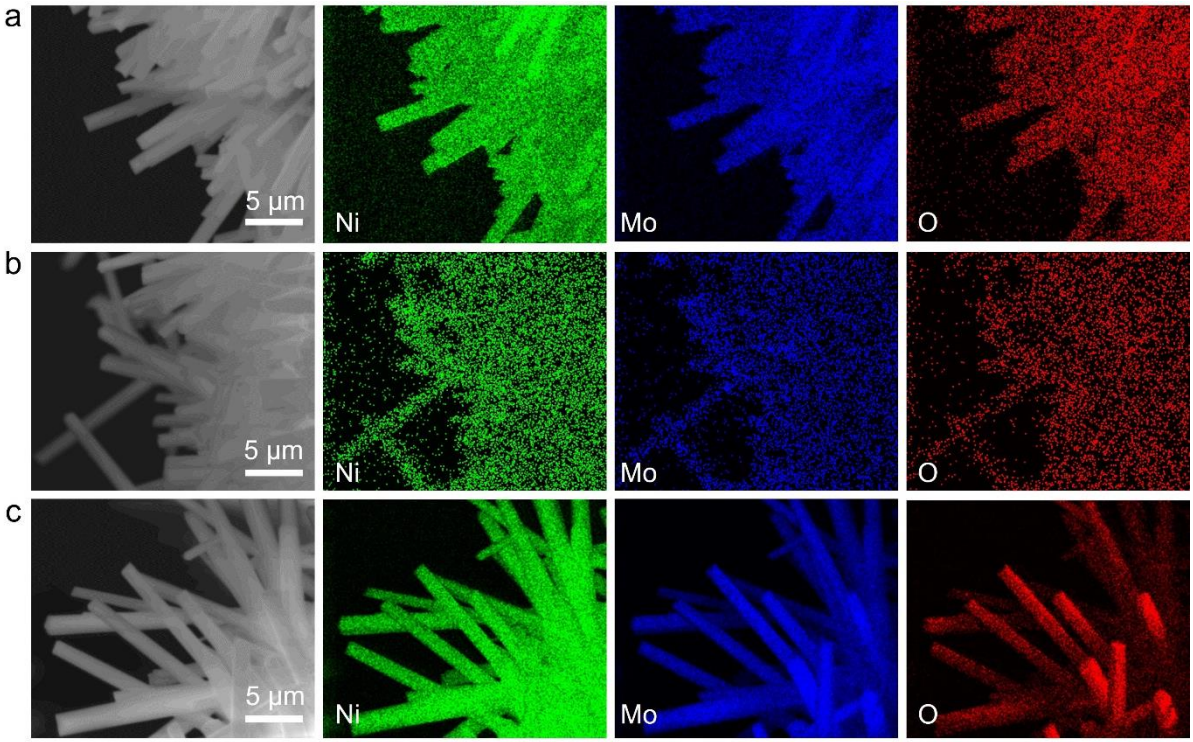

Supplementary Fig. 14 EDS-mapping images of e-$NiMoO_4$ with different sizes (a, 3 × 3 cm, b, 6 × 6 cm and c, 6 × 20 cm).

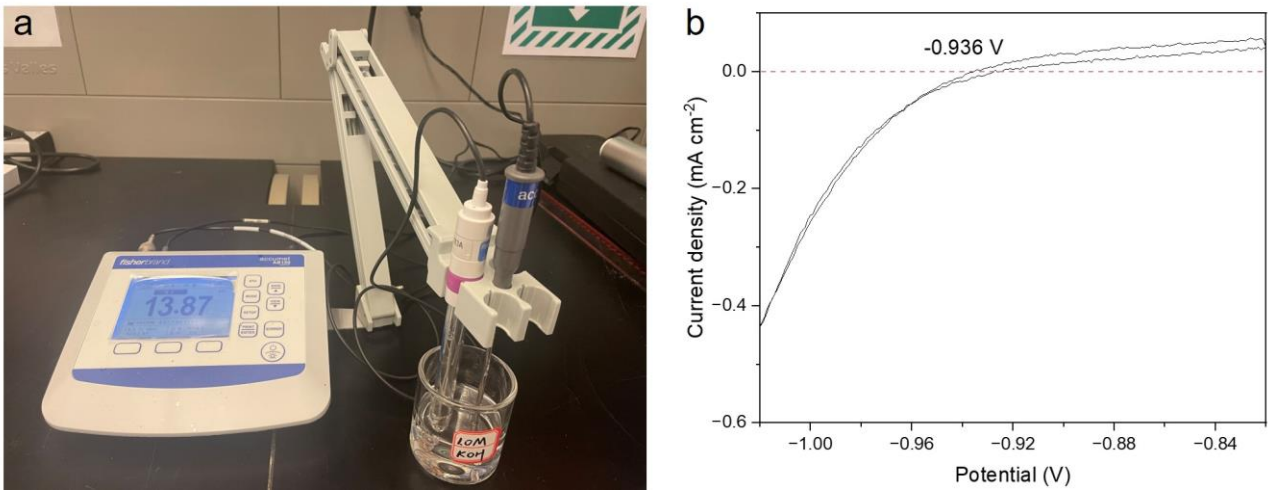

Supplementary Fig. 15 a, Photograph of pH testing. **b,** Calibration of the reference Hg/HgO electrode.

The calibration was performed in a high purity hydrogen-saturated 1.0 M KOH electrolyte with a Pt wire as the working electrode, Hg/HgO as the reference electrode and Pt wire as the counter electrode. CV was run at a scan rate of 1 mV s^{-1}, and the current crossed zero was taken to be the thermodynamic potential for the hydrogen electrode reactions.

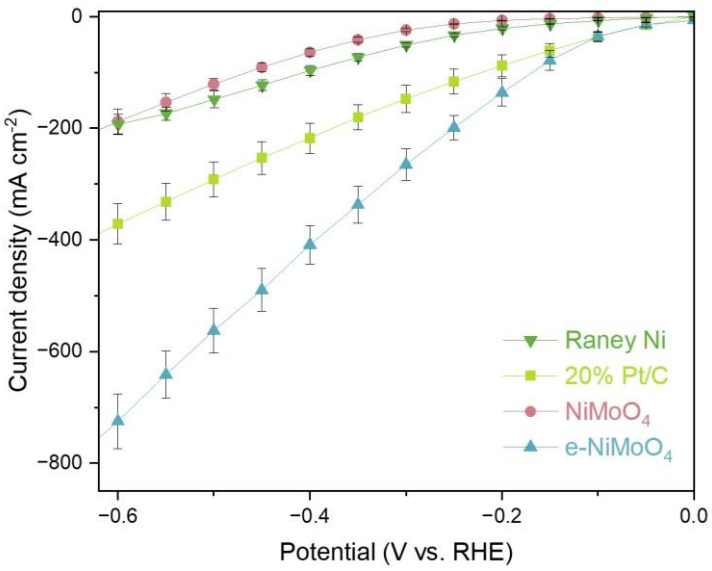

Supplementary Fig. 16 Polarization curves with error bars of e-$NiMoO_4$ and control samples (scan rate 5 mV s^{-1}).

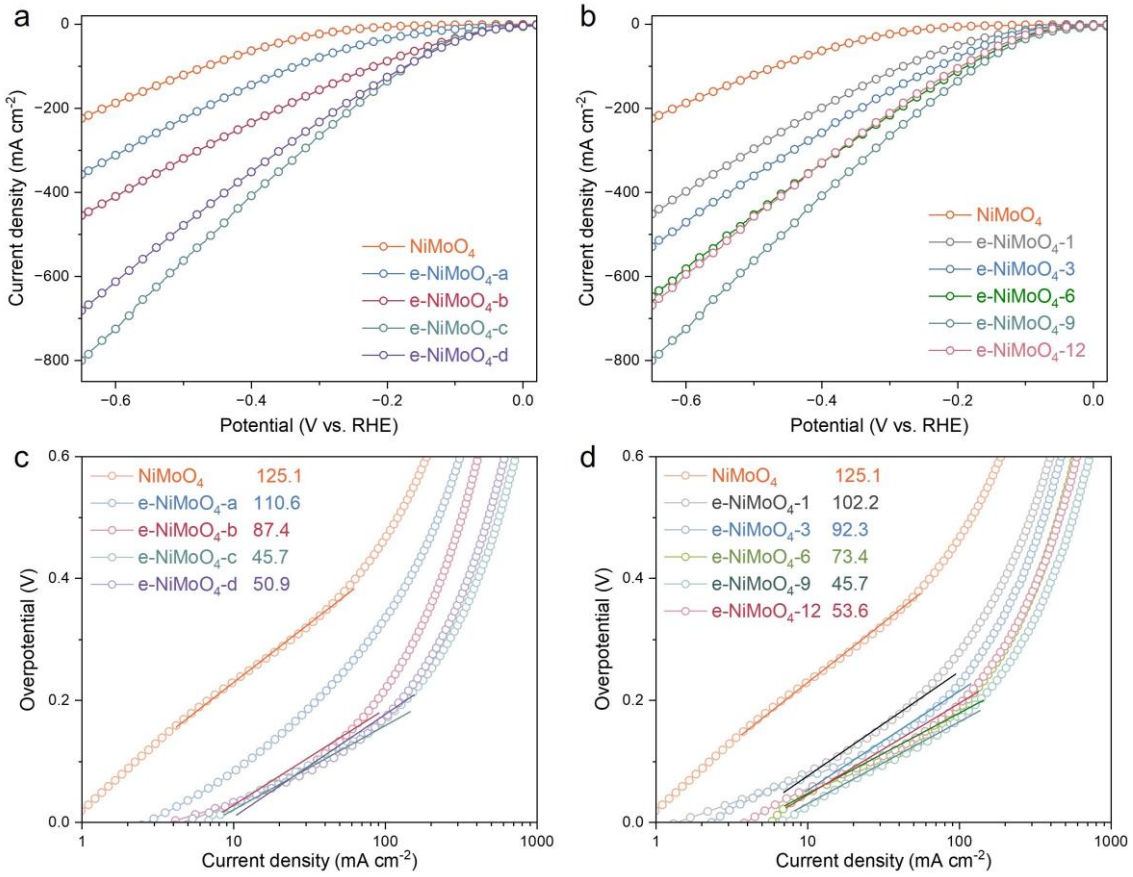

Supplementary Fig. 17 a, Polarization curves of $NiMoO_4$ and e-$NiMoO_4$ with different reconstruction potential (e-$NiMoO_4$-a, -0.085 V; e-$NiMoO_4$-a, -0.285 V; e-$NiMoO_4$-a, -0.485 V; e-$NiMoO_4$-a, -0.685 V;), **c,** Corresponding tafel analysis of **a**. **b,** Polarization curves of $NiMoO_4$ and e-$NiMoO_4$ with different reconstruction time (e-$NiMoO_4$-1, 1 min; e-$NiMoO_4$-3, 3 min; e-$NiMoO_4$-6, 6 min; e-$NiMoO_4$-9, 9 min; e-$NiMoO_4$-12, 12 min), **d,** Corresponding tafel analysis of **c**.

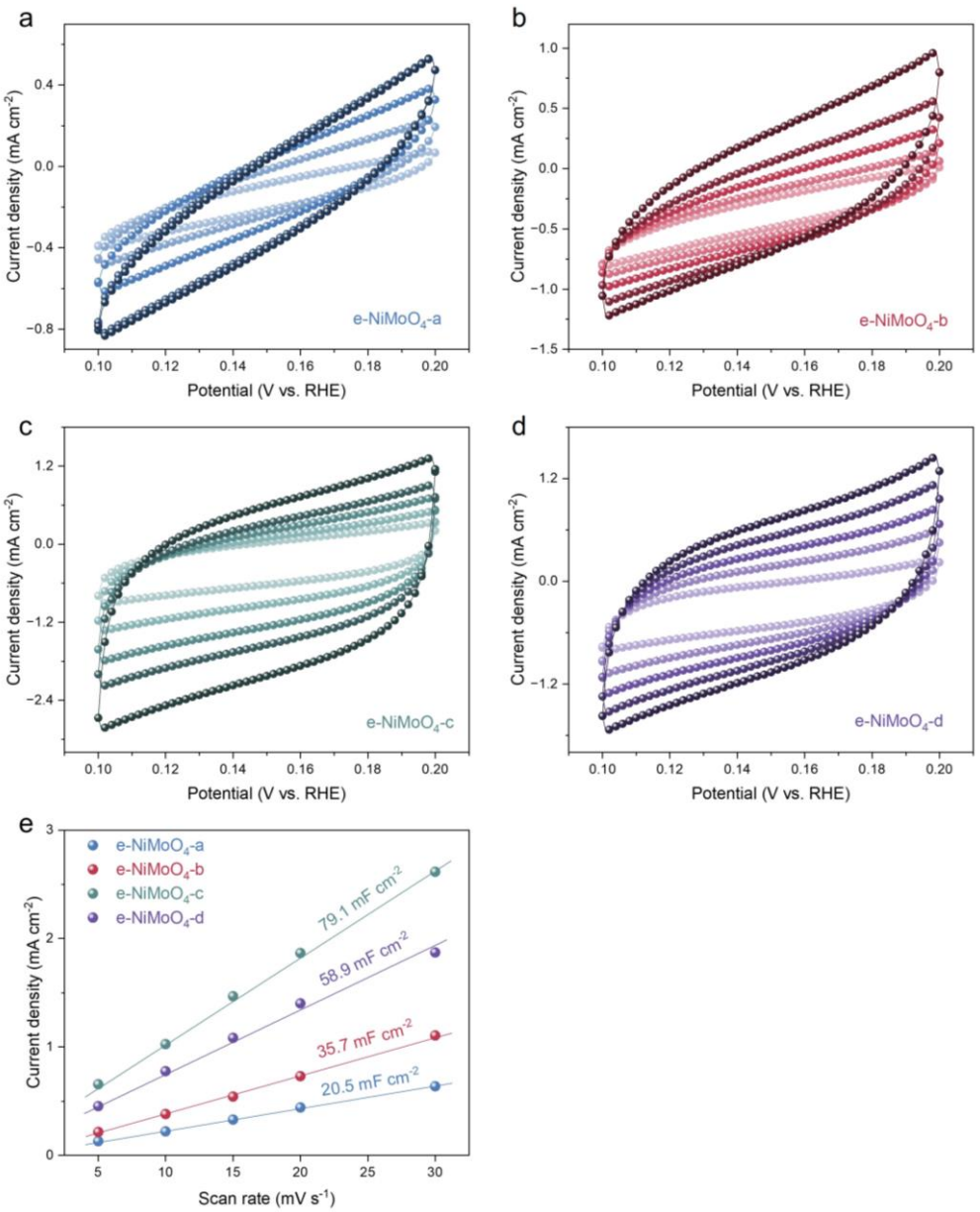

Supplementary Fig. 18 Multiple-measured CV curves of E-$NiMoO_4$ with different reconstruction potential. **a,** e-$NiMoO_4$-a. **b,** e-$NiMoO_4$-b. **c,** e-$NiMoO_4$-c. **d,** e-$NiMoO_4$-d. **e,** Corresponding C_{dl} of above four samples.

With increasing voltage and synthesis time, the electrochemical active surface area (ECSA) of e-$NiMoO_4$ gradually increases (Supplementary Fig. 18-20). ECSA decreases under excessively high synthesis voltages, possibly due to thickening of hydroxide layer and the disappearance of surface dendritic structures at high voltages, aligning with previous morphological characterization.

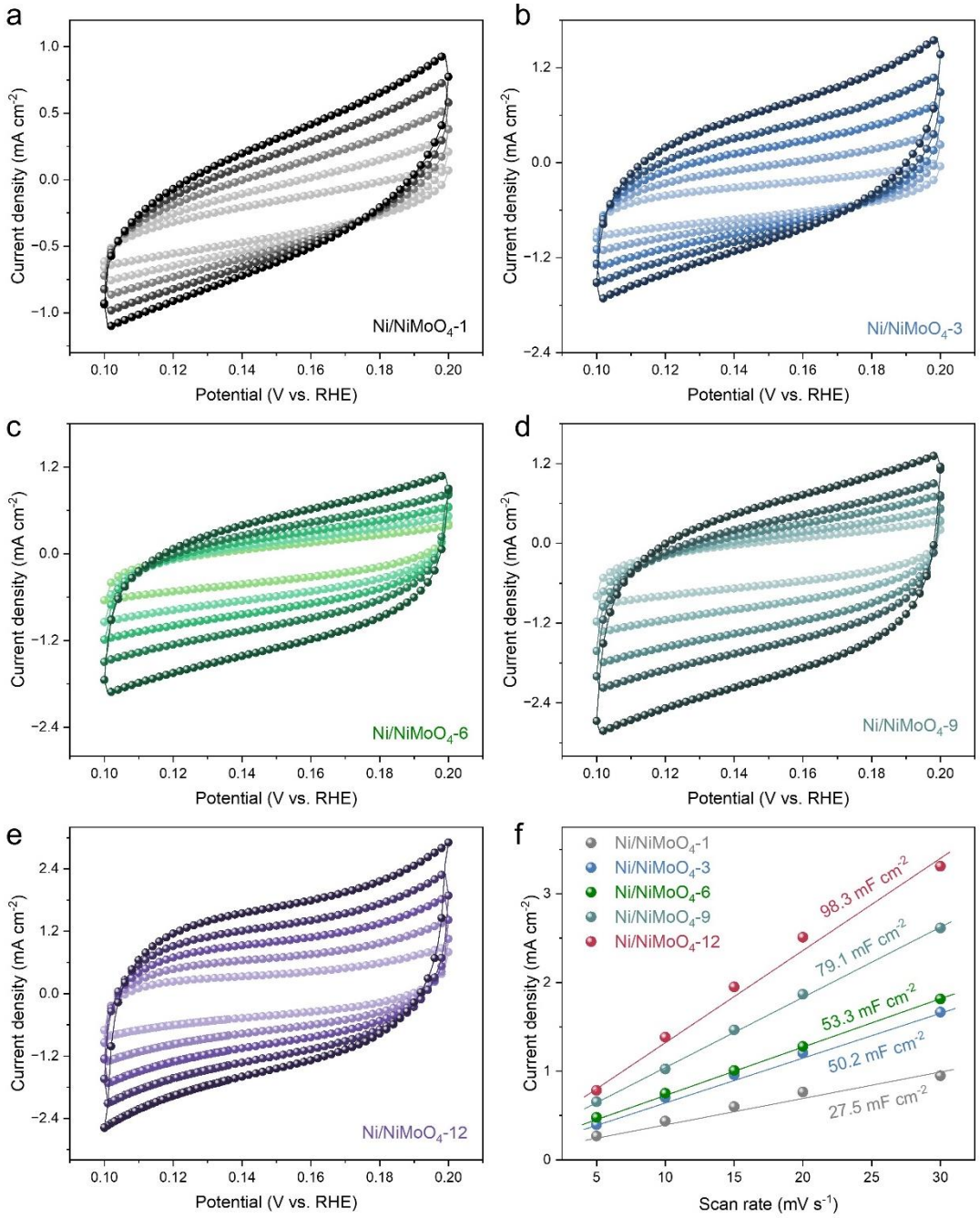

Supplementary Fig. 19 Multiple-measured CV curves of e-$NiMoO_4$ with different reconstruction time. **a,** e-$NiMoO_4$-1. **b,** e-$NiMoO_4$-3. **c,** e-$NiMoO_4$-6. **d,** e-$NiMoO_4$-9. **e,** e-$NiMoO_4$-12. **f,** Corresponding C_{dl} of above five samples.

With increasing reconstruction time (from 1 min to 12 min), the surface roughness significantly increases, indicating that the epitaxial hydroxide layer effectively enhances the surface area[5]. The

electrochemical surface area (ECSA) gradually increases from 27.5 mF cm^{-2} to 98.3 mF cm^{-2}, demonstrating a direct correlation between the roughness induced by the epitaxial $Ni(OH)_2$ layer and the enhancement of ECSA. The sample with the largest active surface area did not exhibit the highest HER activity, suggesting that in the reaction system, HER activity is optimized through the synergistic modulation of the $Ni(OH)_2$-$NiMoO_4$ interfacial structure and ECSA.

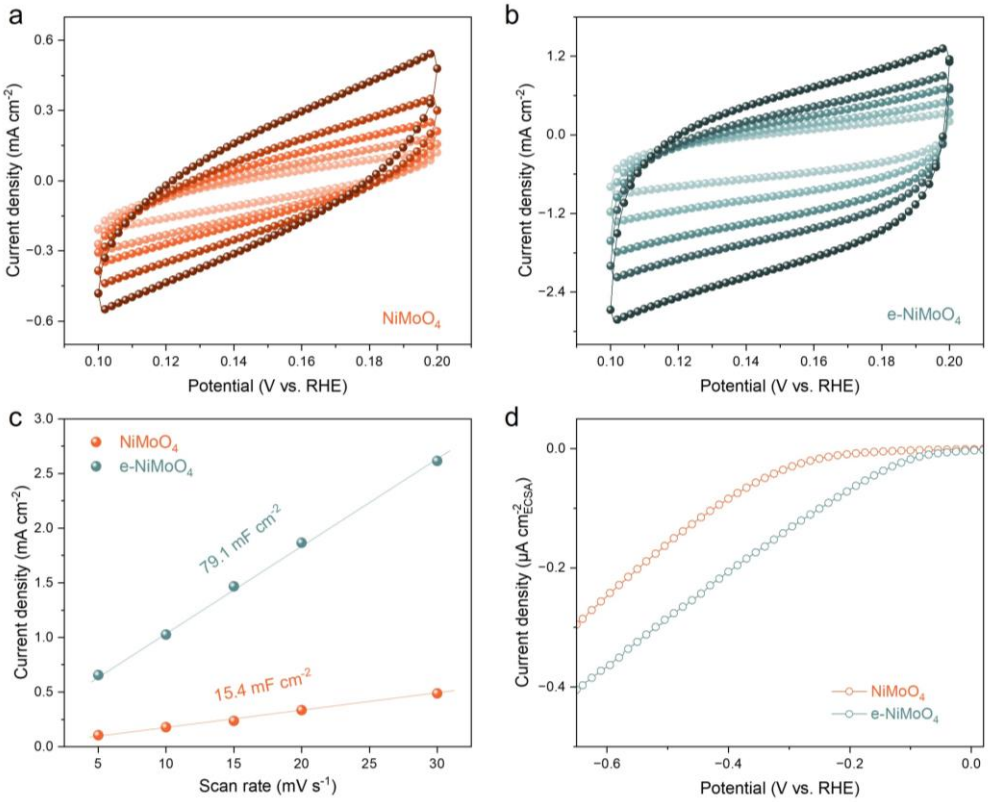

Supplementary Fig. 20 a, Multiple-measured CV curves of $NiMoO_4$. **b,** Multiple-measured CV curves of e-$NiMoO_4$. **c,** Corresponding C_{dl} of above two samples. **d,** ECSA normalized polarization curves of above two samples.

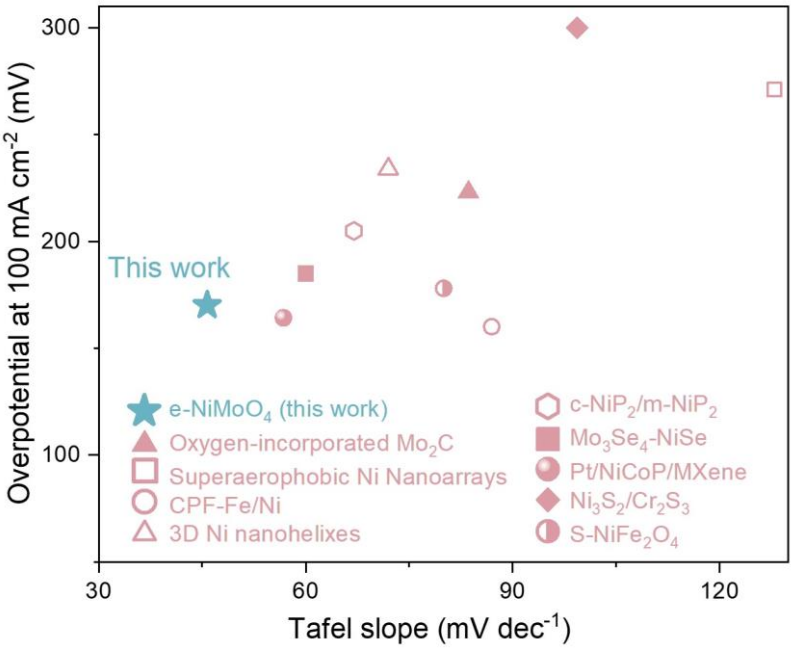

Supplementary Fig. 21 Comparison between e-$NiMoO_4$ and reported catalysts.

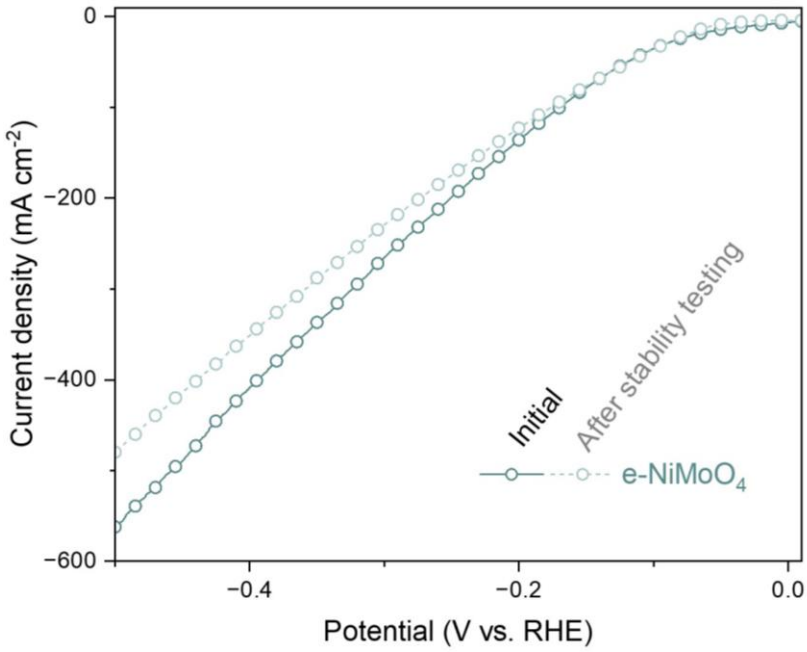

Supplementary Fig. 22 Polarization curves of e-$NiMoO_4$ before and after stability testing.

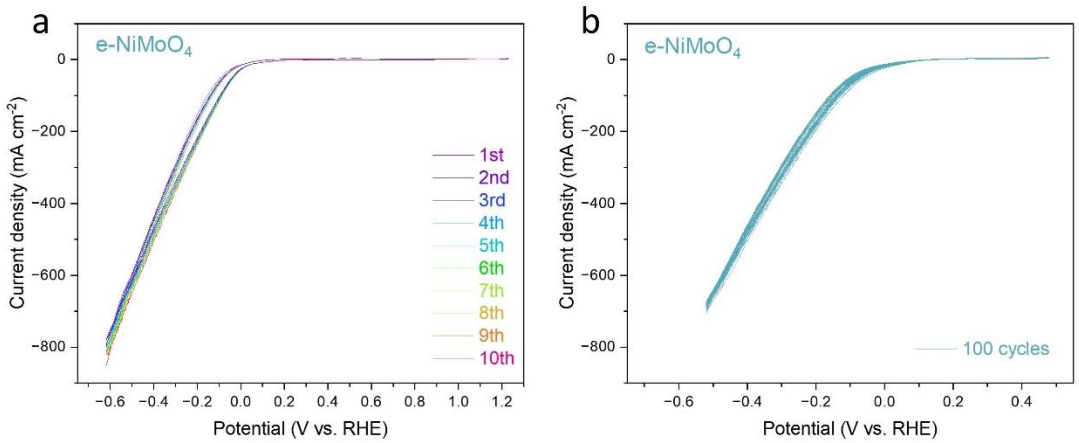

Supplementary Fig. 23 a, Cyclic voltammetry curves of the first ten cycles. **b,** Cyclic voltammetry curves for 100 cycles.

Cyclic voltammetry (CV) cycling tests indicate a slight increase in current density after the first 10 cycles, which can be attributed to improved electrode wettability[6]. After 100 cycles, the material maintains stable activity without noticeable redox peaks, ruling out significant redeposition of dissolved species.

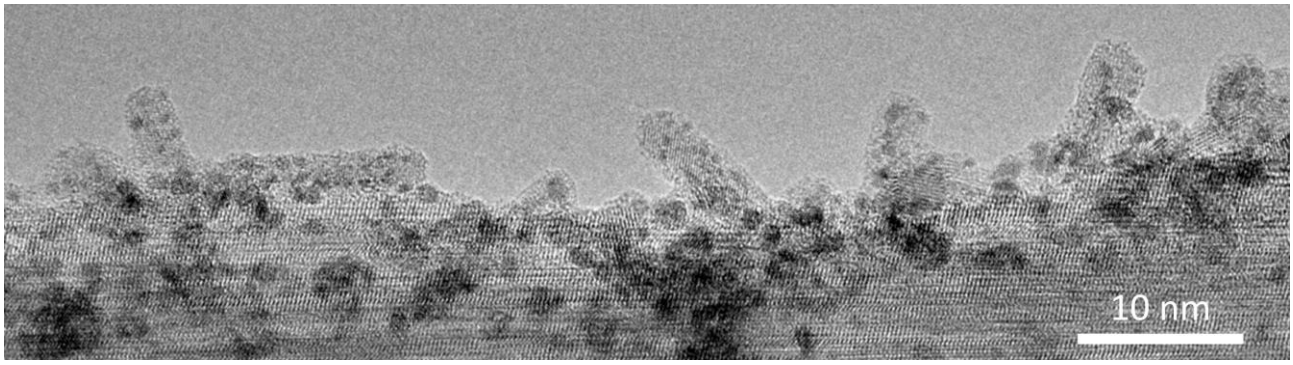

Supplementary Fig. 24 TEM image of e-$NiMoO_4$ after reaction.

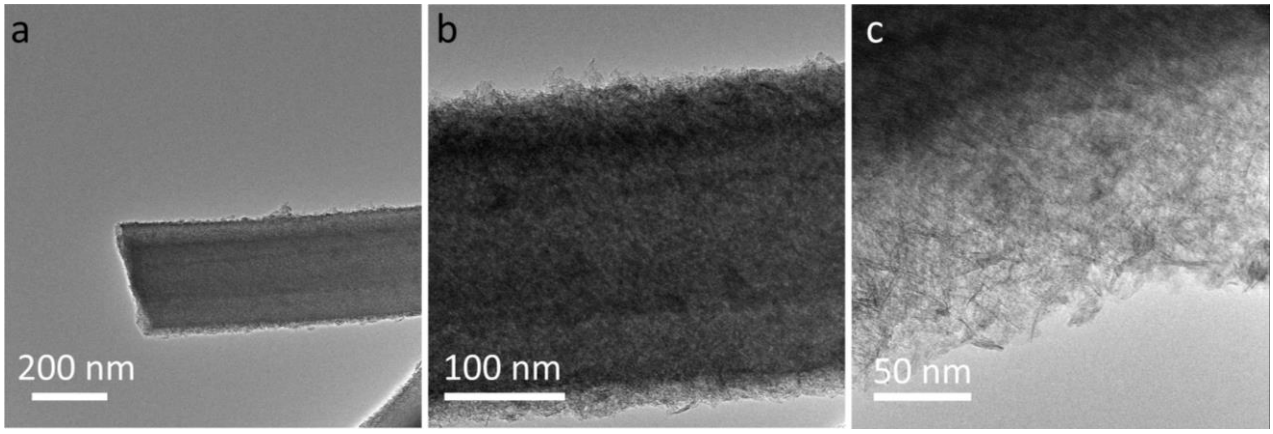

Supplementary Fig. 25 a, b, c, TEM image of e-$NiMoO_4$ after reaction at different magnifications.

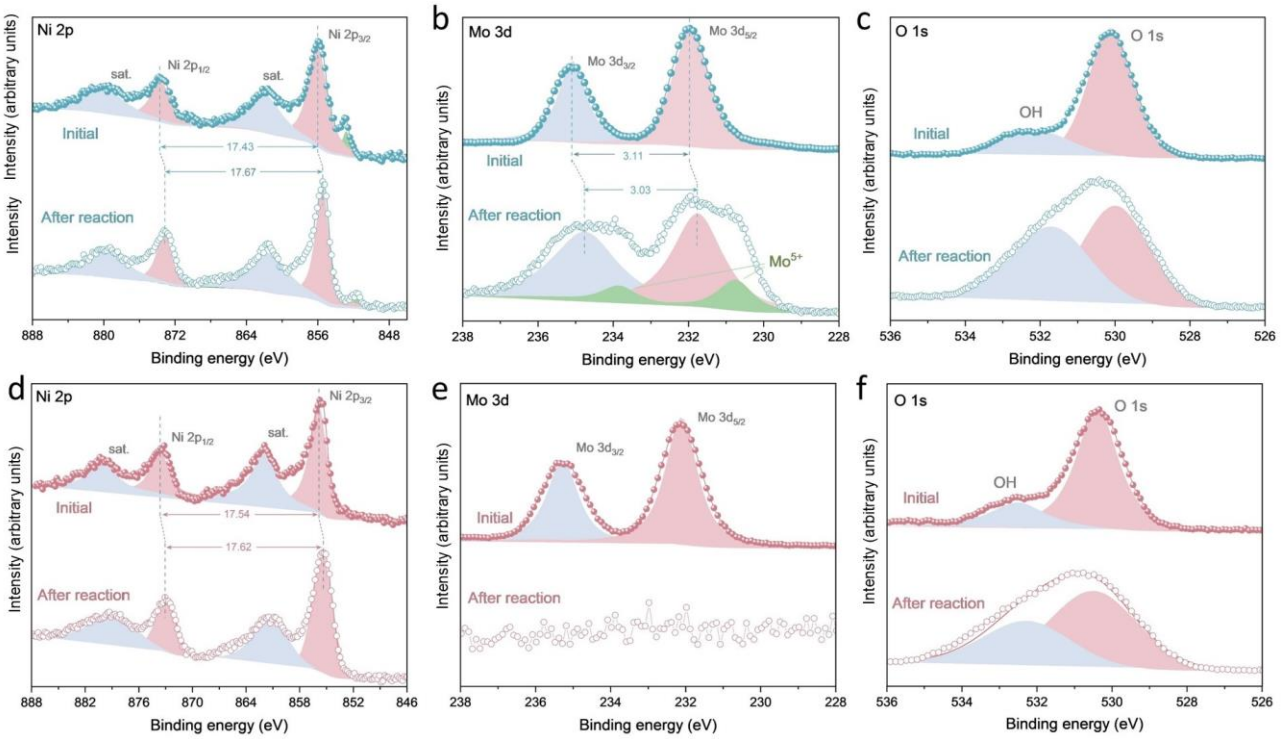

Supplementary Fig. 26 High-resolution XPS spectra of e-$NiMoO_4$ before and after stability testing. **a,** Ni2p. **b,** Mo 3d. **c,** O1s. High-resolution XPS spectra of $NiMoO_4$ before and after stability testing. **d,** Ni2p. **e,** Mo 3d. **f,** O1s.

After the reaction, the oxidation states of both nickel and molybdenum exhibit a downward shift. For $NiMoO_4$, in addition to the shift of the main oxygen peak, a significant increase in OH content is observed upon activation. In the case of e-$NiMoO_4$, the shift in the O 1s peak is attributed to surface hydroxyl passivation.

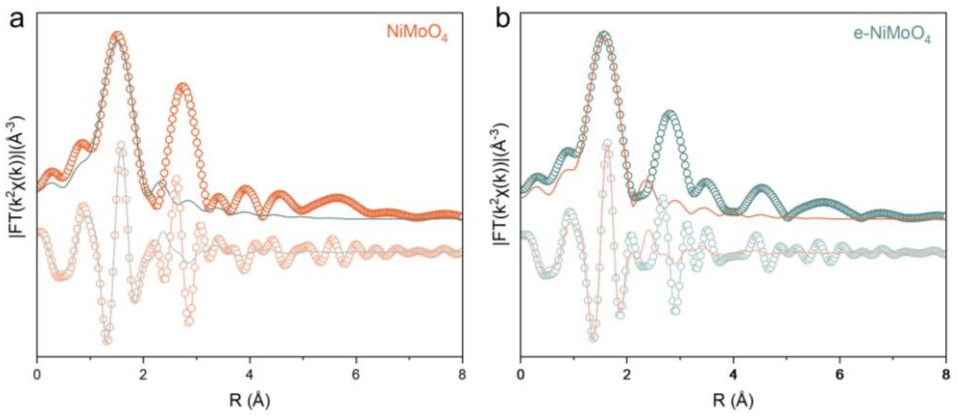

Supplementary Fig. 27 a, Fourier transformed magnitudes of Ni K-edge EXAFS spectra of $NiMoO_4$ after stability testing. **b,** Fourier transformed magnitudes of Ni K-edge EXAFS spectra of e-$NiMoO_4$ after stability testing.

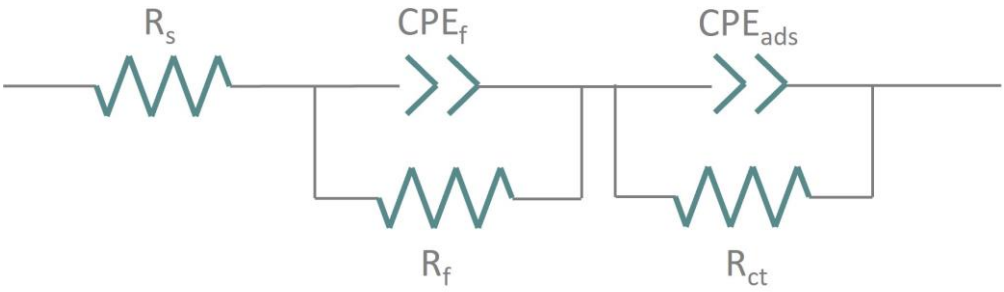

Supplementary Fig. 28 The equivalent circuit diagram of Nyquist plot fitting.

Using the electrochemical reaction parameters mentioned earlier, the voltage range relative to RHE was set from -0.10 to -0.50 V. Upon entering the hydrogen evolution region (-0.20 V), the charge transfer resistance of e-$NiMoO_4$ measures only 7.85 Ω, significantly lower than the 39.4 Ω observed for $NiMoO_4$ at the same potential.

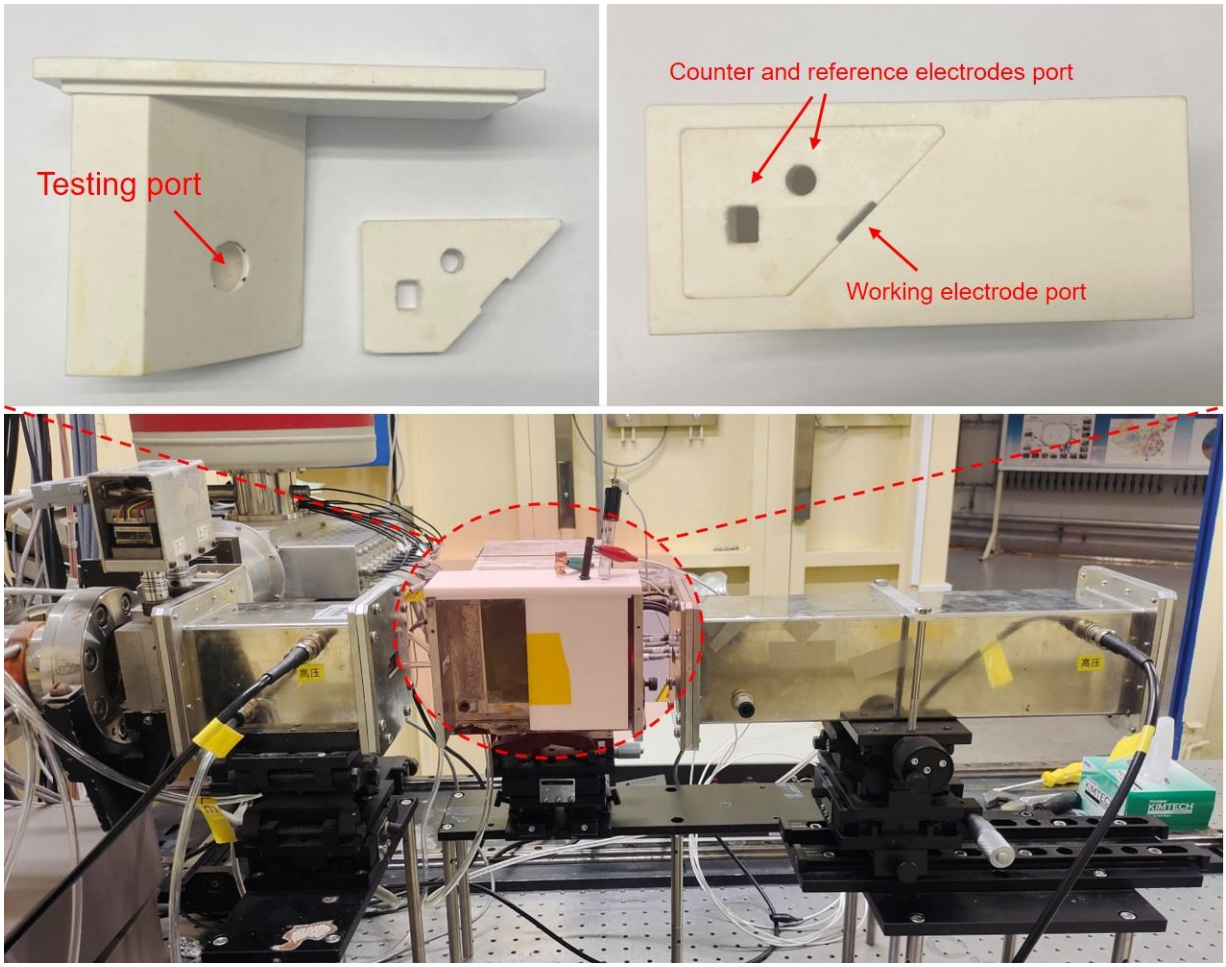

Supplementary Fig. 29 Photographs of the in-situ XAFS testing device and in-situ electrolytic cell.

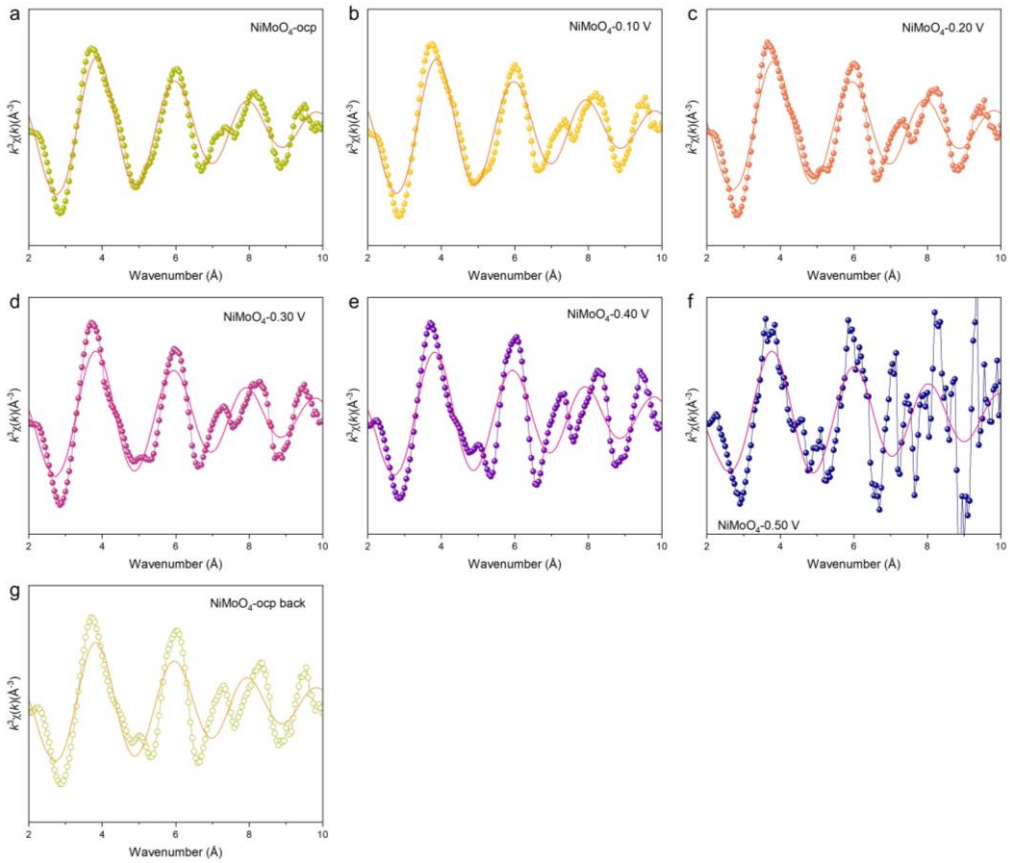

Supplementary Fig. 30 Experimental and best-fitted EXAFS spectra in k space for Ni K-edge of $NiMoO_4$ at different operating potential. **a,** ocp. **b,** -0.10 V. **c,** -0.20 V. **d,** -0.30 V. **e,** -0.40 V. **f,** -0.50 V. **g,** ocp-back.

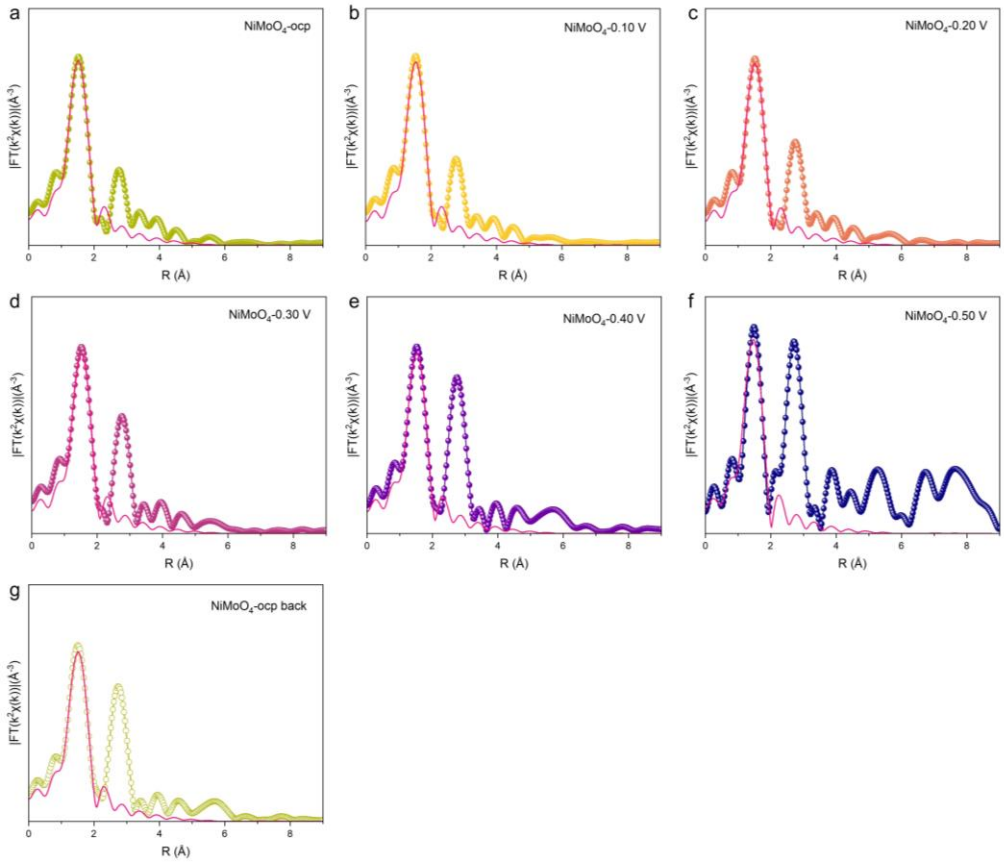

Supplementary Fig. 31 k^2-weighted Fourier transformed EXAFS at the Ni K-edge of $NiMoO_4$ at different operating potential. **a,** ocp. **b,** -0.10 V. **c,** -0.20 V. **d,** -0.30 V. **e,** -0.40 V. **f,** -0.50 V. **g,** ocp-back.

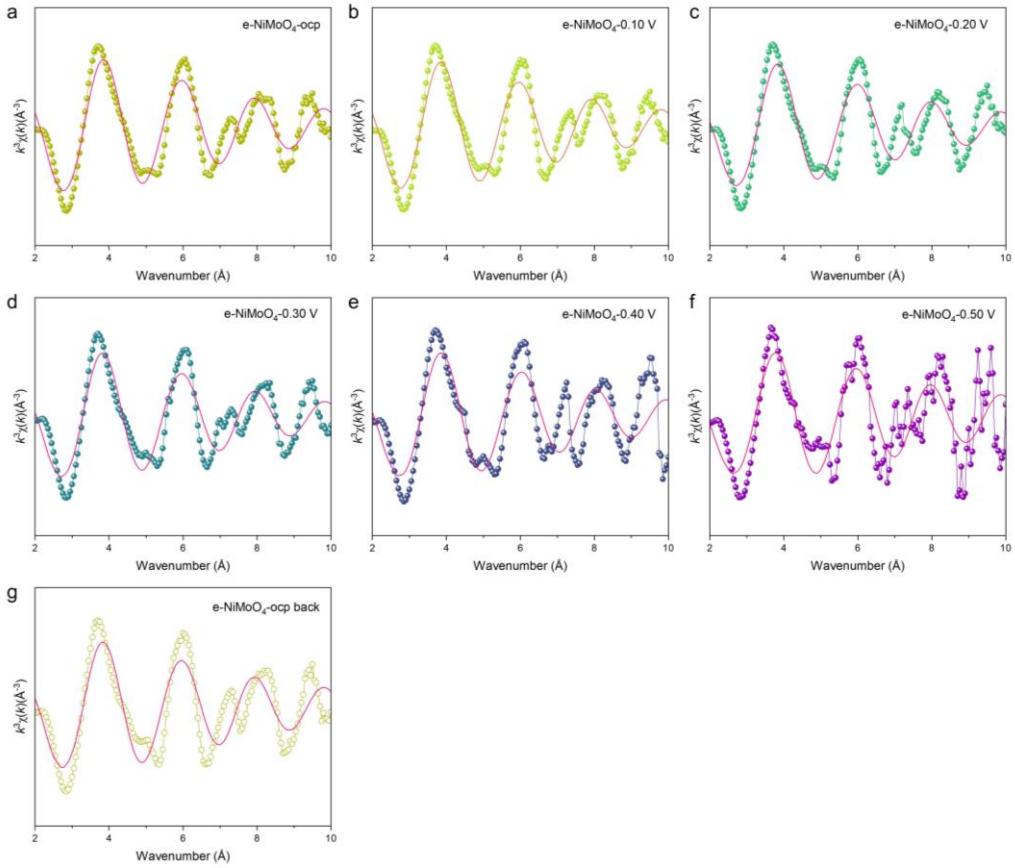

Supplementary Fig. 32 Experimental and best-fitted EXAFS spectra in k space for Ni K-edge of e-$NiMoO_4$ at different operating potential. **a,** ocp. **b,** -0.10 V. **c,** -0.20 V. **d,** -0.30 V. **e,** -0.40 V. **f,** -0.50 V. **g,** ocp-back.

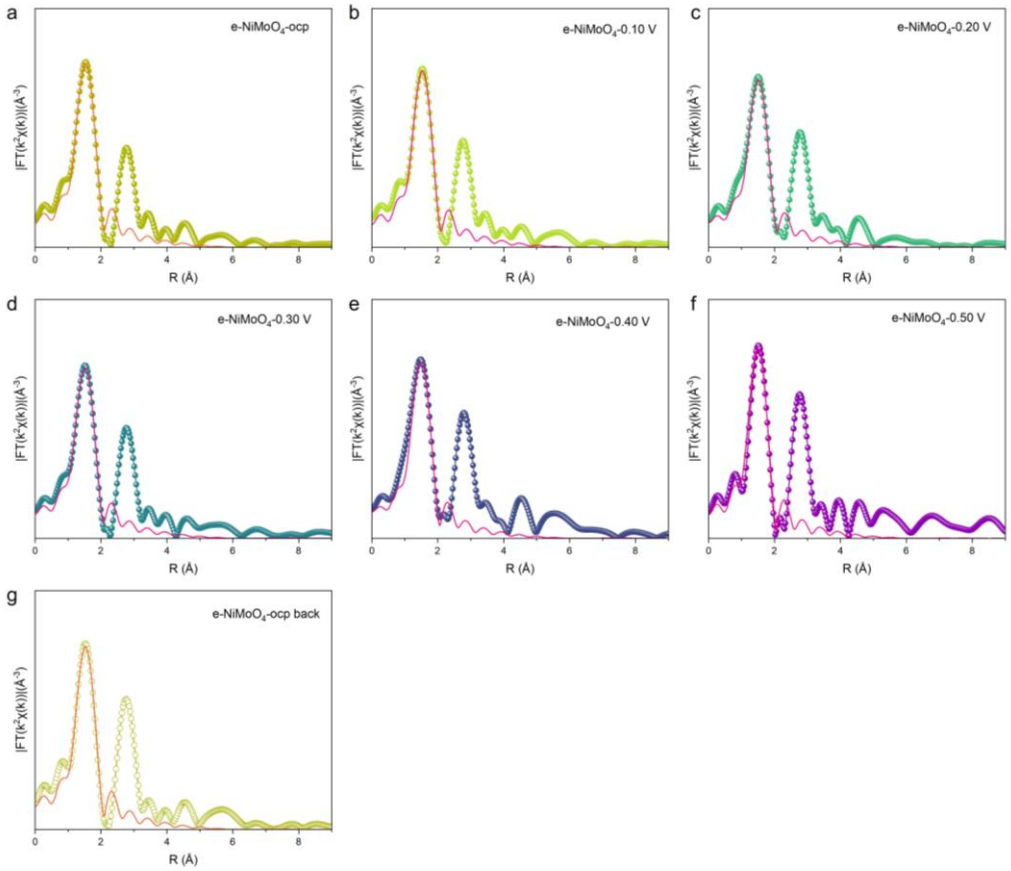

Supplementary Fig. 33 k^2-weighted Fourier transformed EXAFS at the Ni K-edge of e-$NiMoO_4$ at different operating potential. **a,** ocp. **b,** -0.10 V. **c,** -0.20 V. **d,** -0.30 V. **e,** -0.40 V. **f,** -0.50 V. **g,** ocp-back.

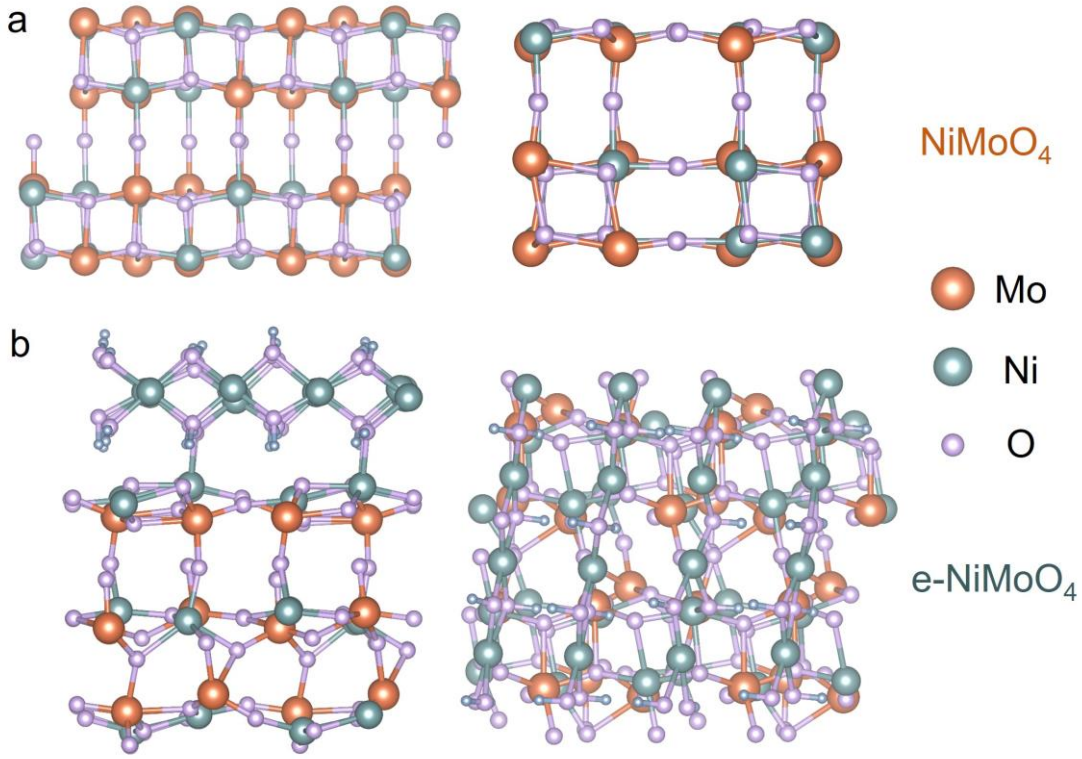

Supplementary Fig. 34 The side view and top view of the theoretical model of $NiMoO_4$ (**a**) and e-$NiMoO_4$ (**b**).

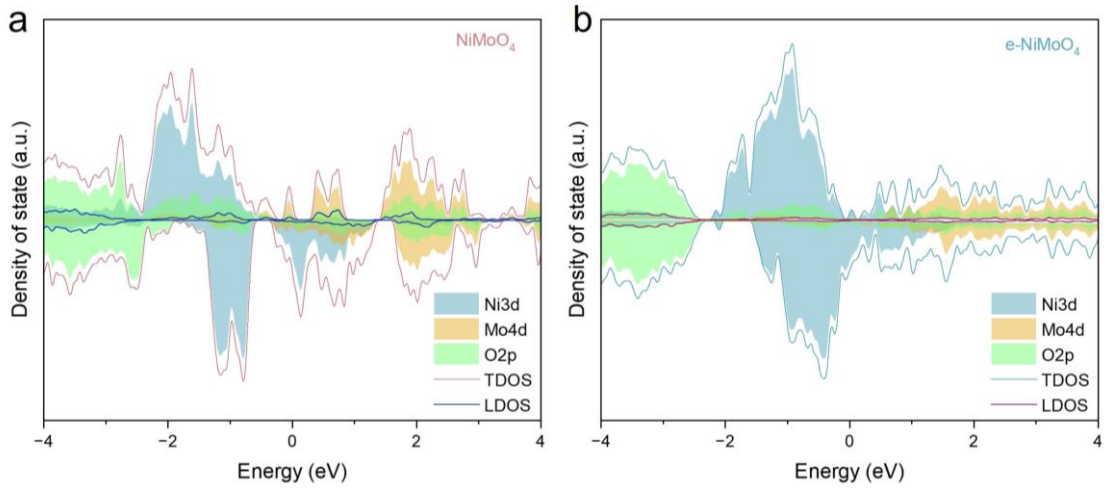

Supplementary Fig. 35 Calculated projected density of states of $NiMoO_4$ (**a**) and e-$NiMoO_4$ (**b**) with total density of states and local density of states.

Projected density of states (PDOS) analysis based on the slab model confirms the presence of low-coordination surface oxygen atoms. The PDOS results confirm that these oxygen atoms at the bottom of slab models contribute minimally to the electronic states near the Fermi level, which shows that the constructed slab model is reasonable. The typical indicator (O*2p* band center and $\Delta_{O2p,Ni3d}$) are negative and exhibit minimal differences, indicating that oxygen is chemically inert and does not serve as an active site. Through strong bonding interactions with neighboring Ni and Mo atoms, these oxygen atoms stabilize the epitaxial interface, thereby preventing lattice distortion during the HER process.

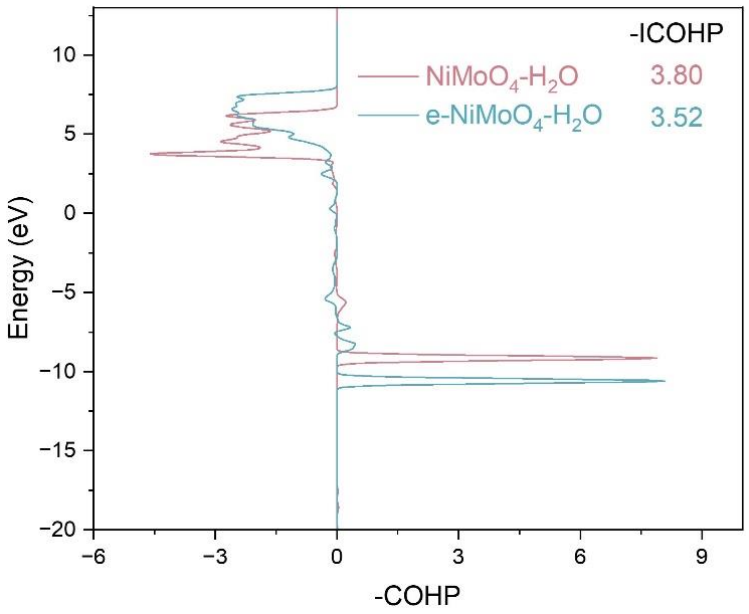

Supplementary Fig. 36 Crystal orbital Hamilton population (COHP) analysis of the O-H bond in the adsorbed OH* for $NiMoO_4$ and e-$NiMoO_4$.

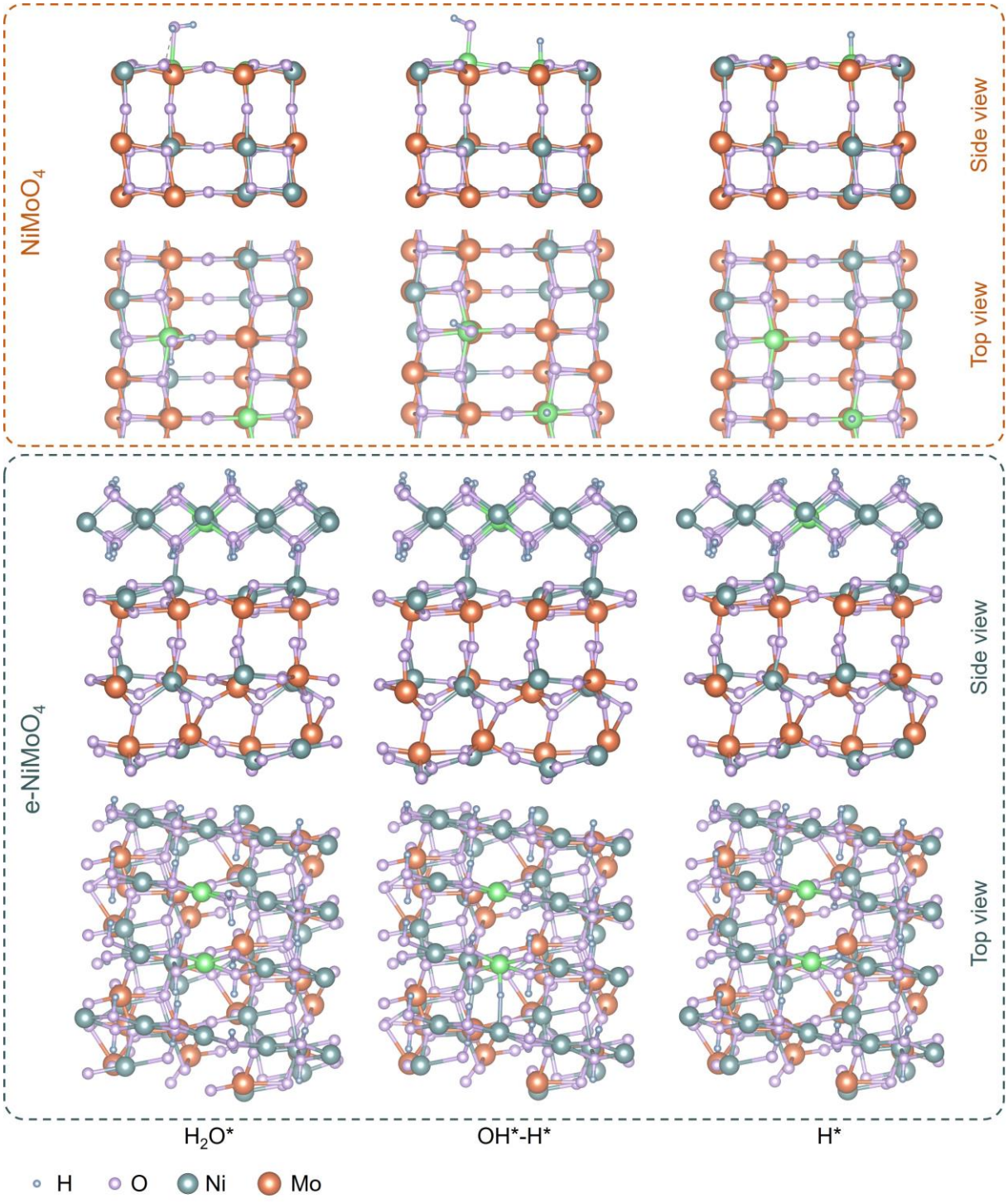

Supplementary Fig. 37 The theoretical models of different adsorption reaction groups on $NiMoO_4$ and e-$NiMoO_4$.

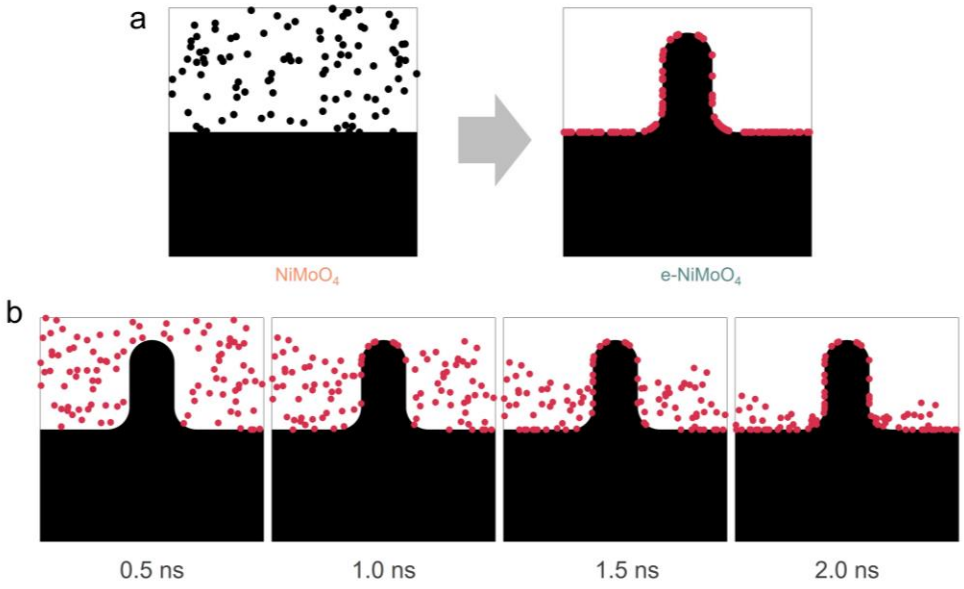

Supplementary Fig. 38 a, The comparison of K ion absorption on $NiMoO_4$ and e-$NiMoO_4$. **b**, Comsol simulation of K ion absorption in e-$NiMoO_4$ over different time.

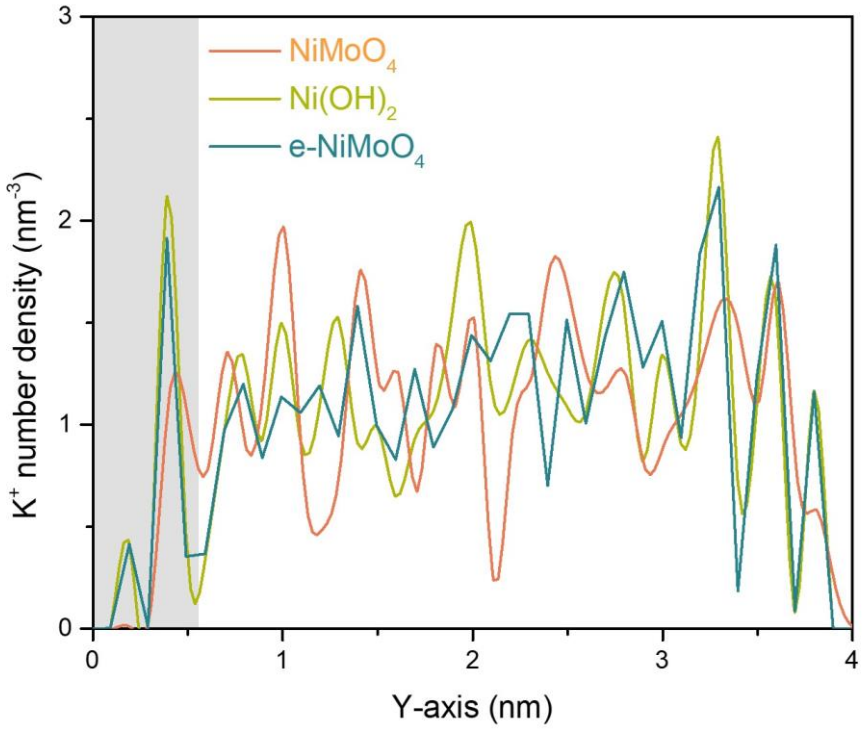

Supplementary Fig. 39 Radial distribution density of potassium ions.

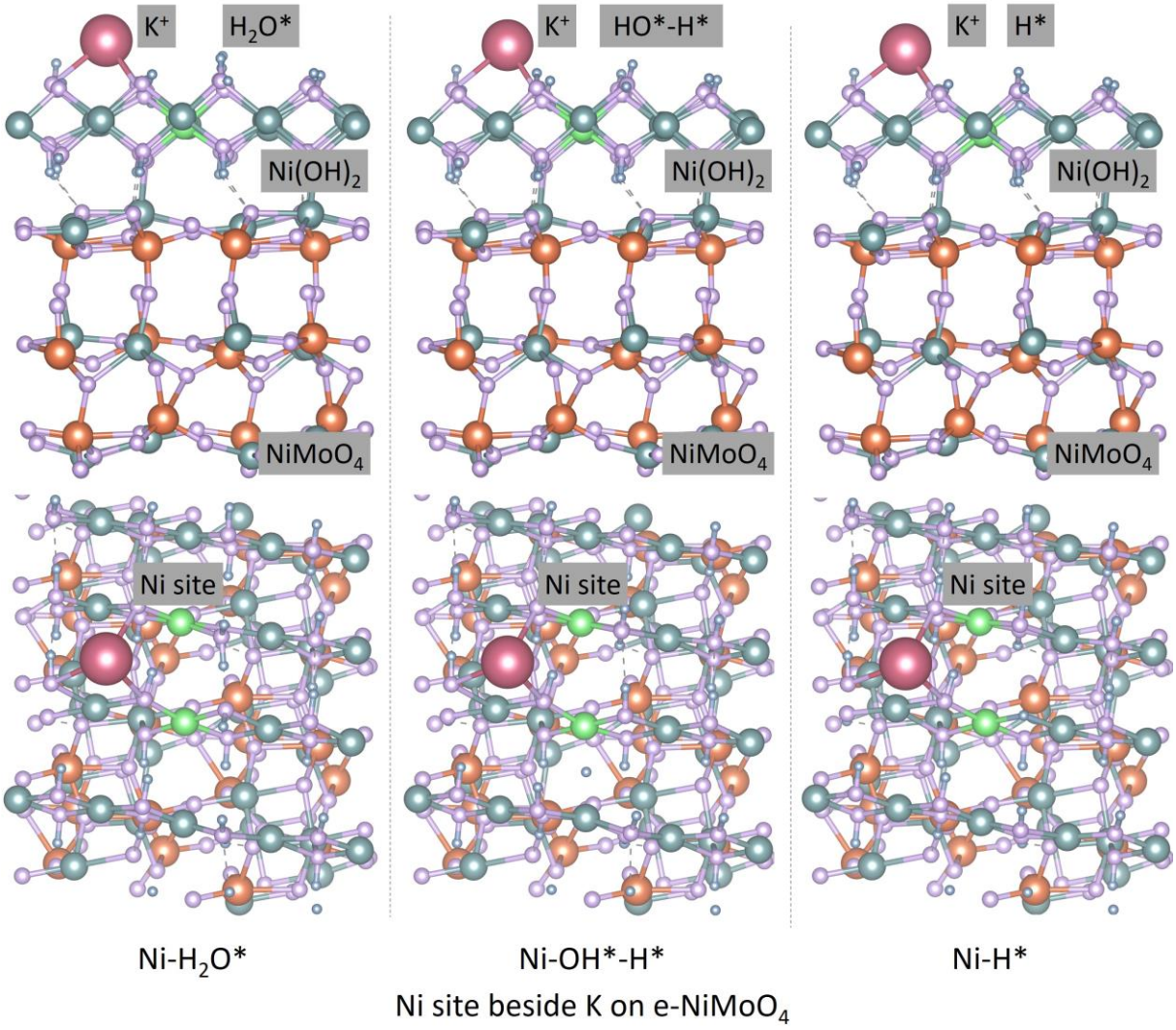

Supplementary Fig. 40 The theoretical models of different adsorption reaction groups on nickel site beside K ion on e-$NiMoO_4$.

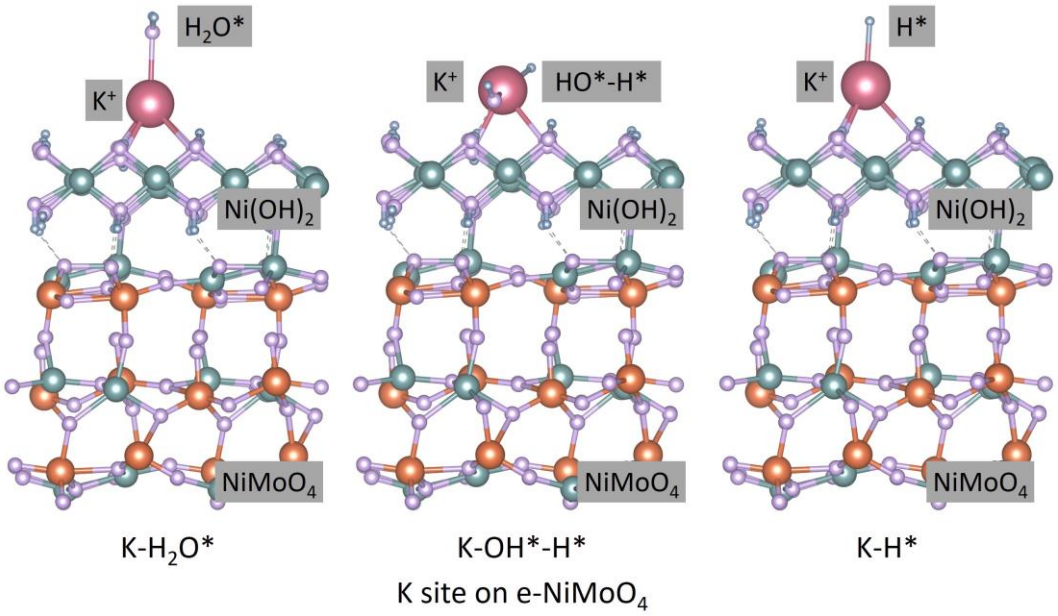

Supplementary Fig. 41 The theoretical models of different adsorption reaction groups on K sites on e-$NiMoO_4$.

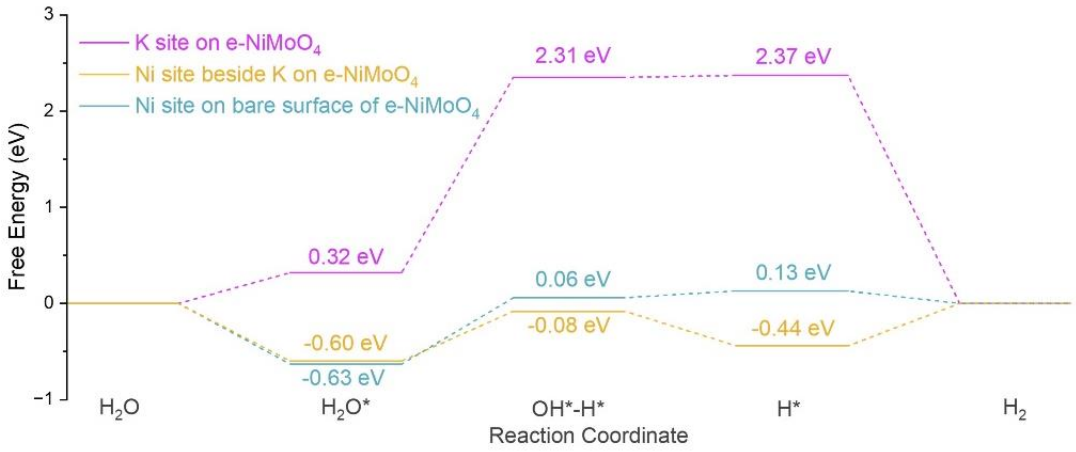

Supplementary Fig. 42 Free energy profile for the alkaline HER process on different sites on e-$NiMoO_4$.

To elucidate the detailed mechanism by which K^+ optimizes the alkaline HER pathway, we introduced K^+ ions near the active sites. On the e-$NiMoO_4$ surface, the dissociation barrier of H_2O is 0.69 eV, primarily due to the sluggish cleavage of the O-H bond[7]. The water activation barrier on K sites on e-$NiMoO_4$ remains excessively high, limiting its catalytic efficiency. In contrast, at the Ni site adjacent to K^+, the free energy barrier for the conversion of H_2O to OH-H is reduced, thereby facilitating faster OH*-H* decoupling[8]. Overall, the synergistic effect of K^+ is evident in the free energy landscape. While K^+ lowers the Volmer barrier, its primary role lies in rebalancing the H* adsorption–desorption equilibrium, which aligns well with experimental observations.

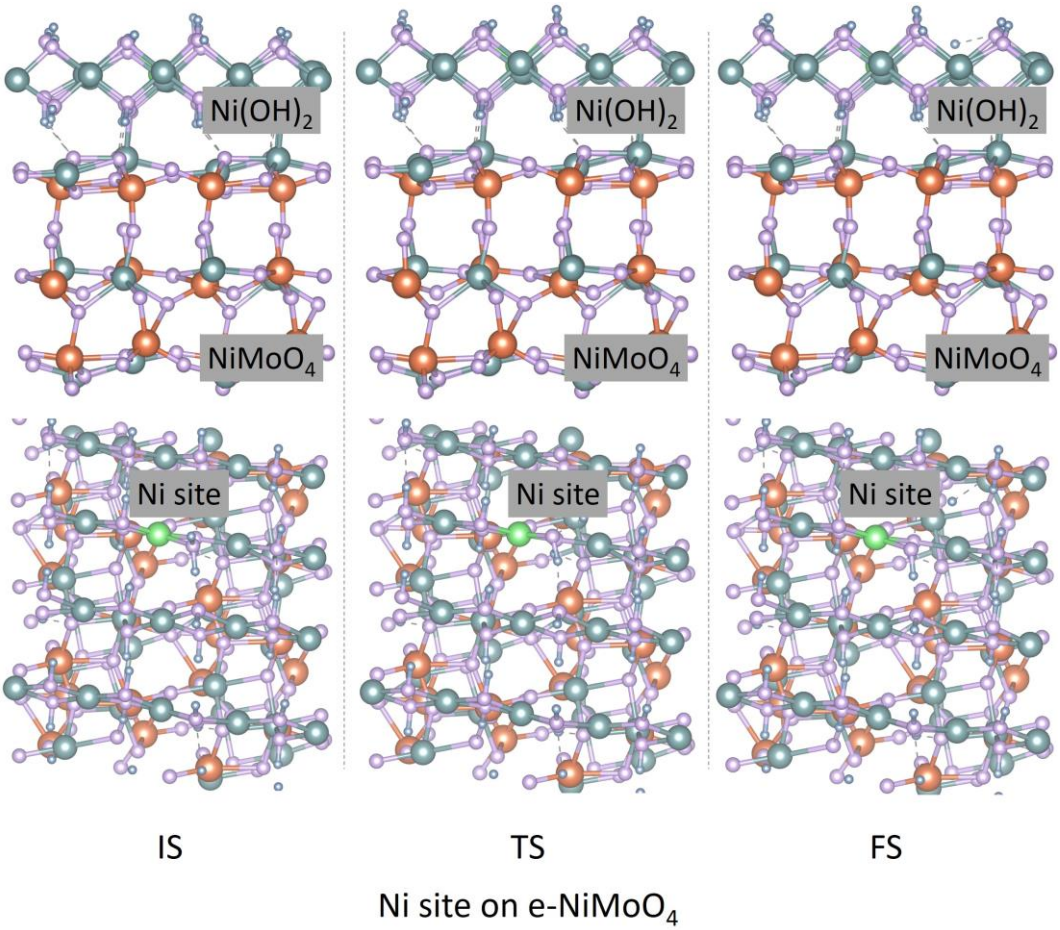

Supplementary Fig. 43 The theoretical models of different reaction state on nickel sites of e-$NiMoO_4$.

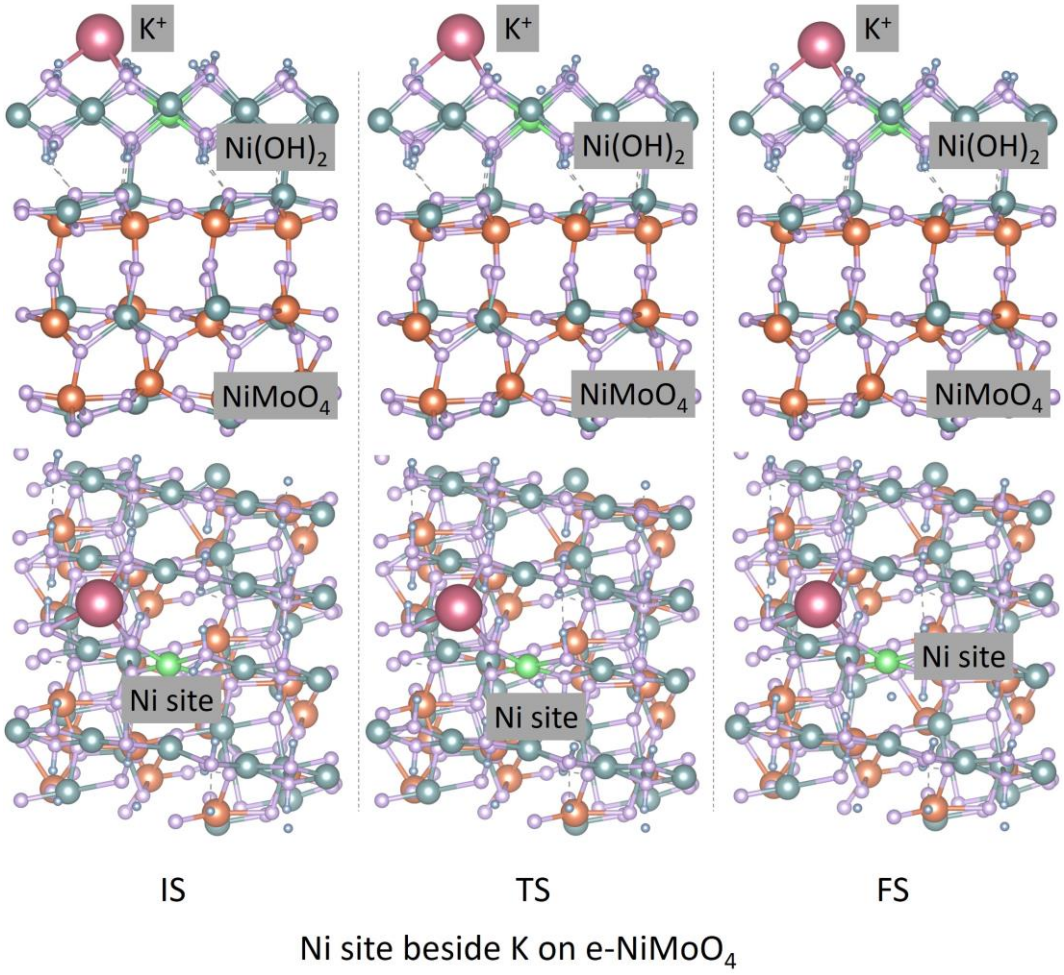

Supplementary Fig. 44 The theoretical models of different reaction state on nickel sites beside K of e-$NiMoO_4$.

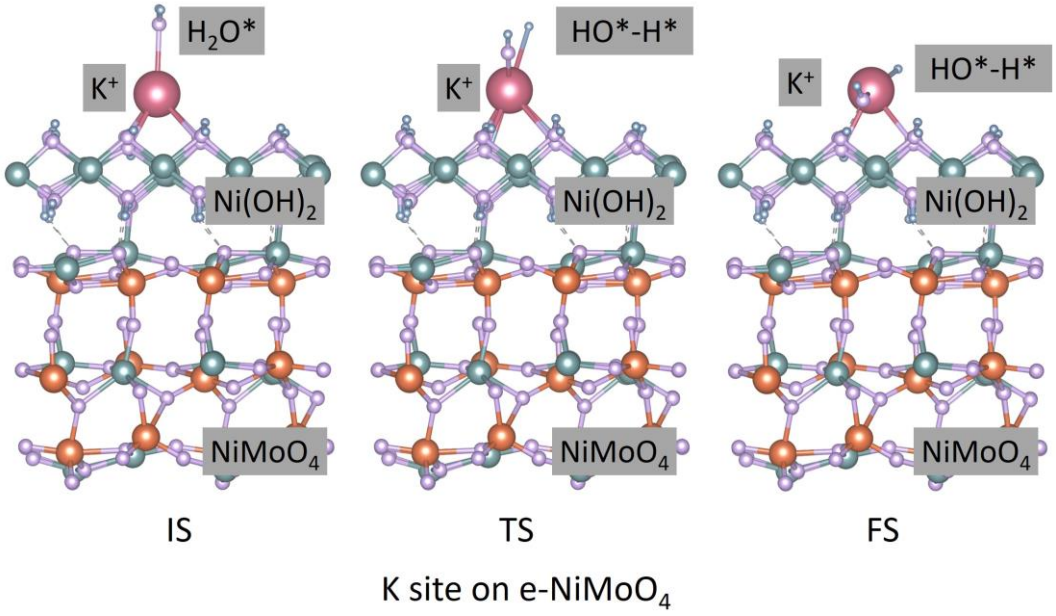

Supplementary Fig. 45 The theoretical models of different reaction state on K sites of e-$NiMoO_4$.

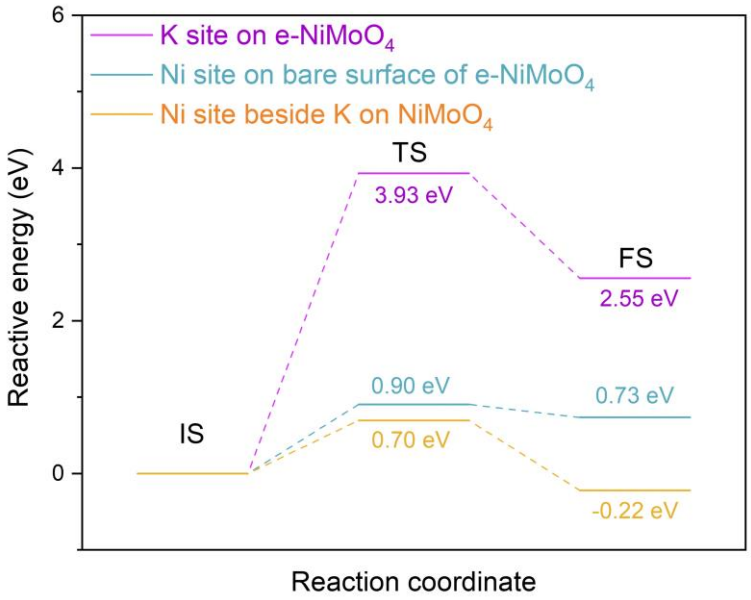

Supplementary Fig. 46 Transition state analysis at different active sites.

Transition state energy analysis revealed significant differences in the dissociation pathway of H_2O into OH^- and H* at the nickel site (bare surface of e-$NiMoO_4$), nickel site (beside K on e-$NiMoO_4$), and the K^+ adsorption site (K site on e-$NiMoO_4$) during alkalin HER. On the nickel site of the bare e- $NiMoO_4$ surface, the transition state energy for H_2O dissociation (TS = 0.90 eV) is relatively low, indicating a lower O–H bond cleavage barrier and faster reaction kinetics[8]. The final state energy (0.73 eV) further confirms the high stability of the dissociated OH^- and H* intermediates, facilitating subsequent reaction steps. In contrast, at the K site, the transition state energy increases significantly (TS = 3.93 eV), with a final state energy of 2.55 eV, much higher than that at the nickel site. This suggests that the stability of the dissociated OH^--H* intermediate is considerably lower, potentially requiring additional energy input to sustain the reaction. Furthermore, at the nickel site adjacent to K^+, the transition state energy barrier is the lowest (0.70 eV), and the final state energy is -0.22 eV. This indicates that the presence of K^+ further reduces the HER energy barrier at the nickel site, enhancing its catalytic activity.

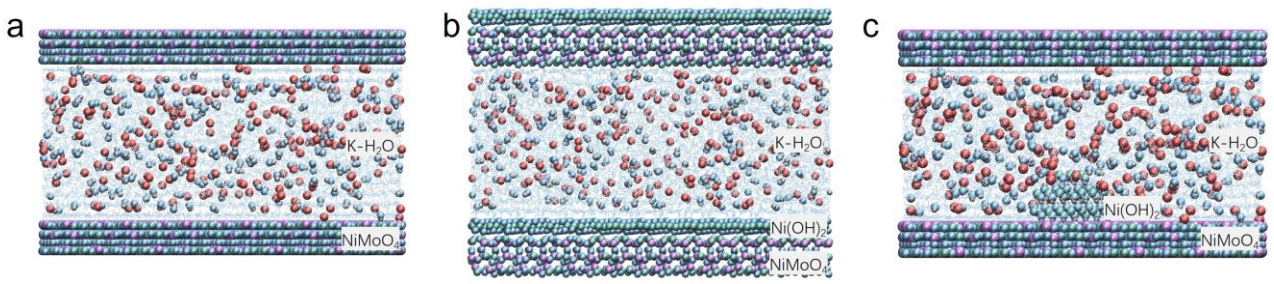

Supplementary Fig. 47 The distribution of K^+ ions and water molecules in the $NiMoO_4$ (a), $Ni(OH)_2$ (b) and e-$NiMoO_4$ models (c).

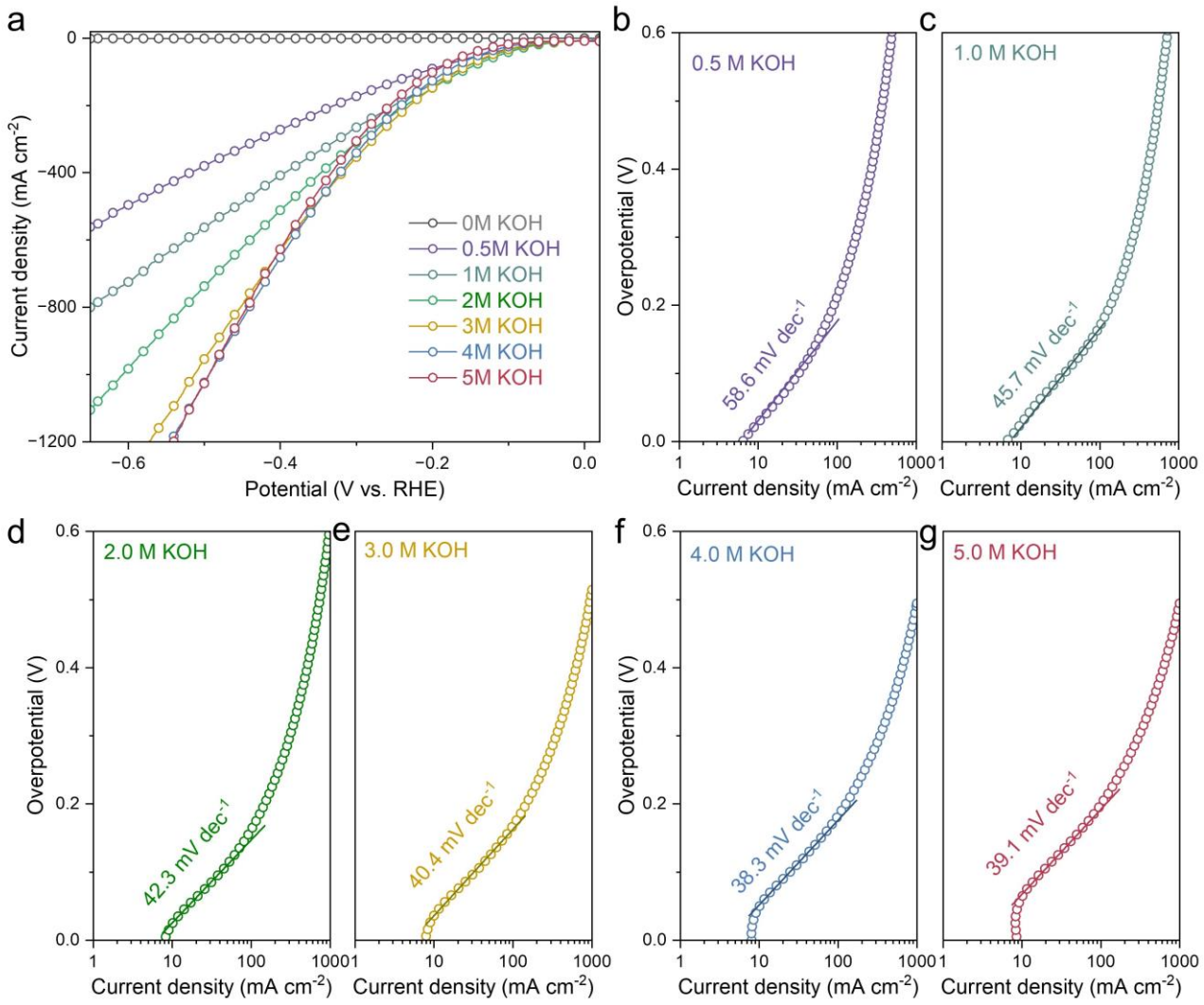

Supplementary Fig. 48 a, Polarization curves of e-NiMoO4 in different concentration KOH solutions. Corresponding tafel analysis of **a**. **b,** 0.5 M KOH. **c,** 1.0 M KOH. **d,** 2.0 M KOH. **e,** 3.0 M KOH. **f,** 4.0 M KOH. **g,** 5.0 M KOH.

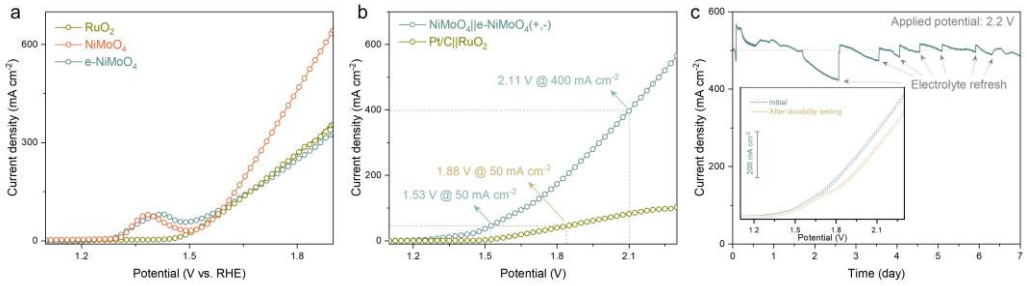

Supplementary Fig. 49 a, OER polarization curves of e-$NiMoO_4$ and control samples. **b,** Polarization curves of e-$NiMoO_4$ in two-electrodes system. **c,** Chronopotentiometry durability test of e-$NiMoO_4$ in two-electrodes system. (The inset shows the comparison of polarization curves before and after stability testing)

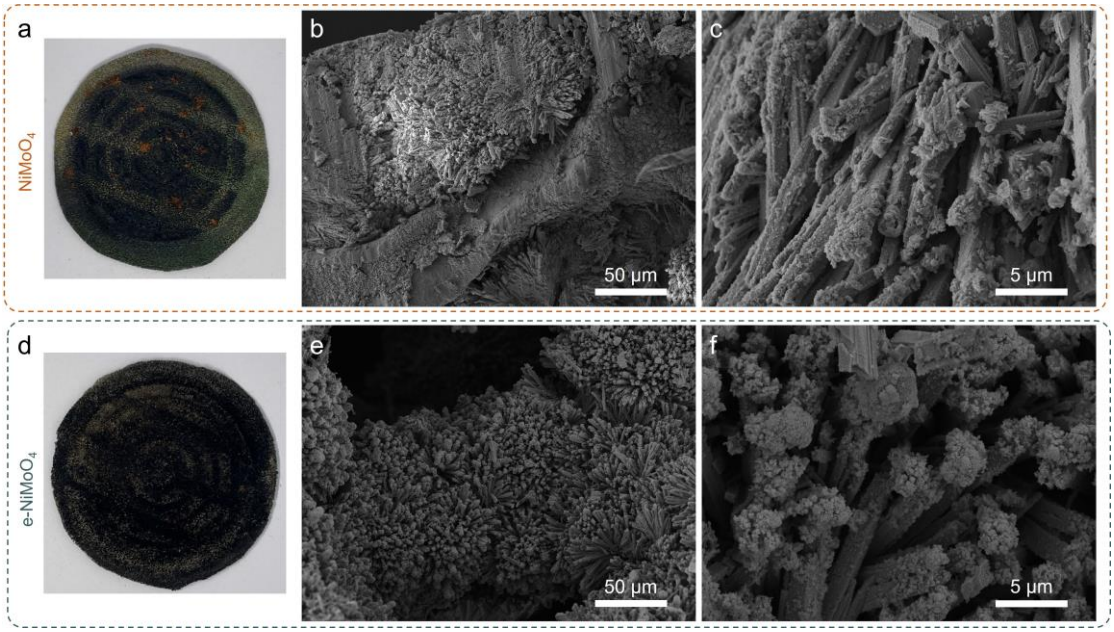

Supplementary Fig. 50 a, b, c, Photo and SEM images of $NiMoO_4$ act as industrial anode electrode after durability testing at different magnification. **d, e, f,** Photo and SEM images of e-$NiMoO_4$ act as industrial cathode electrode after durability testing at different magnification.

Supplementary Table 1. EXAFS fitting parameters at the Ni K-edge for e-$NiMoO_4$ and control samples before and after stability testing.

Sample	*CN*[a]	*R*(Å)[b]	σ^2(Å^2)[c]	*R* factor (%)
Ni foil	12.0	2.48	0.006	0.15
$NiMoO_4$	6.3	2.03	0.006	0.06
$NiMoO_4$-after reaction	5.7	2.03	0.007	0.16
e-$NiMoO_4$	5.5	2.04	0.005	0.23
e-$NiMoO_4$-after reaction	5.3	2.03	0.003	0.62

[a]*CN*, coordination number; [b]*R*, the distance between absorber and backscatter atoms; [c]σ^2, Debye-Waller factor to account for both thermal and structural disorders; *R* factor indicates the goodness of the fit. S_0^2 was fixed to 0.75, according to the experimental EXAFS fit of Ni foil by fixing CN as the known crystallographic value. A reasonable range of EXAFS fitting parameters: $0.700 < S_0^2 < 1.000$; $CN > 0$; $\sigma^2 > 0$ Å^2; *R* factor < 0.02.

Supplementary Table 2. The ICP analysis of metal dissolution behavior under both natural and operational conditions.

Testing Conditions	Electrode Soaking (10 h)		HER Reaction (10 h)	
Materials	$NiMoO_4$	e-$NiMoO_4$	$NiMoO_4$	e-$NiMoO_4$
Dissolved Ni (ppm)	0.31	0.11	0.12	0.09
Dissolved Mo (ppm)	14.0	1.89	7.08	0.85

A portion of Mo in $NiMoO_4$ spontaneously dissolves in an alkaline medium in the form of molybdate. The corresponding ICP results confirm that after immersing a 1.5×1 cm $NiMoO_4$ sample in 20 mL of 1.0 M KOH with stirring for 10 hours, the Mo concentration in the solution was 14.0 ppm.

Supplementary Table 3. EXAFS fitting parameters at the Ni K-edge for $NiMoO_4$ at different potentials.

Sample	*CN*[a]	*R*(Å)[b]	σ^2(Å^2)[c]	*R* factor (%)
$NiMoO_4$-ocp	6.1	2.03	0.005	0.16
$NiMoO_4$-0.1V	5.7	2.03	0.005	0.17
$NiMoO_4$-0.2V	5.7	2.03	0.005	0.26
$NiMoO_4$-0.3V	5.4	2.03	0.004	0.27
$NiMoO_4$-0.4V	5.2	2.03	0.004	0.17
$NiMoO_4$-0.5V	5.4	1.99	0.003	0.23
$NiMoO_4$-ocp back	5.2	2.02	0.004	0.16

[a]*CN*, coordination number; [b]*R*, the distance between absorber and backscatter atoms; [c]σ^2, Debye-Waller factor to account for both thermal and structural disorders; *R* factor indicates the goodness of the fit. S_0^2 was fixed to 0.75, according to the experimental EXAFS fit of Ni foil by fixing CN as the known crystallographic value. A reasonable range of EXAFS fitting parameters: $0.700 < S_0^2 < 1.000$; $CN > 0$; $\sigma^2 > 0$ Å^2; *R* factor < 0.02.

Supplementary Table 4. EXAFS fitting parameters at the Ni K-edge for e-$NiMoO_4$ at different potentials.

Sample	*CN*[a]	*R*(Å)[b]	σ^2(Å^2)[c]	*R* factor (%)
e-$NiMoO_4$-ocp	5.5	2.03	0.004	0.13
e-$NiMoO_4$-0.1V	5.4	2.03	0.005	0.20
e-$NiMoO_4$-0.2V	5.4	2.02	0.005	0.30
e-$NiMoO_4$-0.3V	5.5	2.02	0.005	0.13
e-$NiMoO_4$-0.4V	5.3	2.00	0.004	0.14
e-$NiMoO_4$-0.5V	5.2	2.01	0.003	0.90
e-$NiMoO_4$-ocp back	5.3	2.03	0.004	0.16

[a]*CN*, coordination number; [b]*R*, the distance between absorber and backscatter atoms; [c]σ^2, Debye-Waller factor to account for both thermal and structural disorders; *R* factor indicates the goodness of the fit. S_0^2 was fixed to 0.75, according to the experimental EXAFS fit of Ni foil by fixing CN as the known crystallographic value. A reasonable range of EXAFS fitting parameters: $0.700 < S_0^2 < 1.000$; $CN > 0$; $\sigma^2 > 0$ Å^2; *R* factor < 0.02.

Supplementary Table 5. INCAR parameters.

	INCAR-Freq	INCAR-Relax	INCAR-TS
ALGO	Fast	Fast	Normal
ISPIN	2	2	2
IBRION	5	2	3
NSW	300	500	500
EDIFFG	-0.02	-0.02	-0.05
POTIM	0.015	0.1	-
ISIF	2	2	2
IVDW	11	11	11
ISYM	0	0	0
ENCUT	450	450	450
ISMEAR	0	0	0
SIGMA	0.05	0.05	0.05
EDIFF	1e-7	1e-5	1e-5
NELMIN	5	5	5
NELM	300	300	300
GGA	PE	PE	PE
LREAL	Auto	Auto	Auto
MAGMOM	NFREE = 2	40*2 24*2 120*0.1 33*0.1	40*4 24*2 121*0.1 34*0.1 1*0.

Supplementary Table 6. *k*-point optimization parameters.

	K point density	System energy (eV)	Atomic average energy (eV)	Relative energy (eV)
$NiMoO_4$	2 × 2 × 1	-1030.8672	-7.5799	
	3 × 3 × 1	-1030.7413	-7.5790	0.0009
	4 × 4 × 1	-1030.8692	-7.5799	0.0000
e-$NiMoO_4$	2 × 2 × 1	-1473.5821	-10.8352	
	3 × 3 × 1	-1473.5073	-10.8346	0.0006
	4 × 4 × 1	-1473.3938	-10.8338	0.0014

Supplementary Table 7. *s*,*p*,*d*-center of $NiMoO_4$ and e-$NiMoO_4$.

$NiMoO_4$	Spin-Channel	s band center (eV)	p band center (eV)	d band center (eV)
Mix	Spin-up	-6.311	-3.908	-1.660
	Spin-down	-6.279	-3.772	-0.795
Ni	Spin-up	-2.264	-2.784	-2.438
	Spin-down	-2.329	-2.695	-0.966
Mo	Spin-up	-6.732	-6.876	-0.780
	Spin-down	-6.657	-6.859	-0.605
O	Spin-up	-6.918	-3.400	-
	Spin-down	-6.855	-3.240	-
e-$NiMoO_4$	Spin-Channel	s band center (eV)	p band center (eV)	d band center (eV)
Mix	Spin-up	-7.110	-4.111	-1.346
	Spin-down	-7.106	-4.040	-0.860
Ni	Spin-up	-2.785	-2.535	-1.579
	Spin-down	-2.828	-2.485	-0.862
Mo	Spin-up	-7.699	-7.805	-0.903
	Spin-down	-7.669	-7.770	-0.857
O	Spin-up	-7.941	-3.670	-
	Spin-down	-7.923	-3.591	-

Supplementary Table 8. The specific values of the zero-point energy (ZPE) and transition state (TS) for each reaction intermediate during the Gibbs free energy calculations.

$NiMoO_4$	$*H_2O$	*OH+*H	*H
ΔE_{ZPE}	0.7379	0.5920	0.2203
$T\Delta S$	0.1038	0.0003	0.0090
e-$NiMoO_4$	$*H_2O$	*OH+*H	*H
ΔE_{ZPE}	0.7222	0.6431	0.1685
$T\Delta S$	0.3702	0.1386	-0.0428
K site e-$NiMoO_4$	$*H_2O$	*OH+*H	*H
ΔE_{ZPE}	0.6777	0.4172	0.0960
$T\Delta S$	0.1443	0.1941	0.1288
Ni site besdie K	$*H_2O$	*OH+*H	*H
ΔE_{ZPE}	0.6667	0.6251	0.1643
$T\Delta S$	0.0912	0.0585	0.0132

Supplementary Reference:

1. Solomon G., *et al.* $NiMoO_4@Co_3O_4$ core–shell nanorods: In situ catalyst reconstruction toward high efficiency oxygen evolution reaction. *Adv. Energy Mater.* **11**, (2021).
2. Jiang R., *et al.* Redox promoted rapid and deep reconstruction of defect-rich nickel precatalysts for efficient water oxidation. *Small* **20**, e2401384 (2024).
3. Zhu Y., *et al.* Multistep dissolution of lamellar crystals generates superthin amorphous $ni(oh)_2$ catalyst for uor. *Adv. Mater.* **35**, e2301549 (2023).
4. Meharban F., *et al.* Scaling up stability: Navigating from lab insights to robust oxygen evolution electrocatalysts for industrial water electrolysis. *Adv. Energy Mater.* **14**, (2024).
5. Davis E. M., Bergmann A., Kuhlenbeck H., Roldan Cuenya B. Facet dependence of the oxygen evolution reaction on Co_3O_4, $CoFe_2O_4$, and Fe_3O_4 epitaxial film electrocatalysts. *J. Am. Chem. Soc.* **146**, 13770-13782 (2024).
6. Liang Y., Han Y., Li J.-s., Wang J., Liu D., Fan Q. Wettability control in electrocatalyst: A mini review. *J. Energy Chem.* **70**, 643-655 (2022).
7. Cui W. G., *et al.* Insights into the ph effect on hydrogen electrocatalysis. *Chem. Soc. Rev.* **53**, 10253-10311 (2024).
8. Yang Y., *et al.* Electrocatalysis in alkaline media and alkaline membrane-based energy technologies. *Chem. Rev.* **122**, 6117-6321 (2022).